STRUCTURING OF GLASS USING ULTRA SHORT NEAR INFRARED LASER PULSES

KTH Engineering Sciences

PATRIK HOLMBERG

Master of Science Thesis
Department of Applied Physics
KTH – Royal Institute of Technology
Stockholm - Sweden 2010

STRUCTURING OF GLASS USING ULTRA SHORT NEAR INFRARED LASER PULSES

Laser Physics
Department of Applied Physics
KTH – Royal Institute of Technology
106 91 STOCKHOLM
Sweden

TRITA-FYS 2010:67
ISSN 0280-316X
ISRN: KTH/FYS/--10:67--SE

Abstract

This thesis deals with structuring glasses, by material ablation or modification of the index of refraction, using short (1 ps) laser pulses with wavelengths in the infrared region ($\lambda \approx 800$ nm). The technique can be used for material modifications in three dimensions for manufacturing complex structures for different types of functional devices, such as Lab-On-A-Chip systems for bio-medical applications, or for integrated optical circuits and components for telecommunication or sensing applications. To enable three-dimensional laser structuring of optical materials with high precision the Laser Physics Groups recently purchased a high-resolution X-Y-Z translation stage system (Aerotech ALS-130) to be integrated with different lasers systems.

The main purpose of this project was to design and construct an experimental setup for laser processing of materials by integrating:

- Laser system (Ti:Sapphire seeded amplifier, 1 ps pulses, wavelength ~800 nm)
- Translation stages (Aerotech ALS-130)
- Suitable optics for beam delivery
- Laser pulse triggering system
- In situ inspection system of sample under processing
- Computer control, user interface and calibration capabilities

Evaluation of the system was performed by structuring commercially available Aluminosilicate glass (Corning® EAGLE2000™). The effects of short, high peak power, pulses in glass were investigated and different microstructures were created (surface ablation and bulk refractive index structures) and evaluated regarding surface/edge smoothness and agreement with the input-design geometry. The ablation threshold and multiple pulse incubation effects of the material, due to irradiance below threshold, were also investigated.

Acknowledgements

I did this work in the Laser physics group at the Department of Applied Physics, KTH. This was a very pleasant time in a driven yet easy going atmosphere. I would like to express my gratitude and thanks to everybody and especially;

Dr Michael Fokine, for the opportunity to do this versatile and interesting work and for excellent supervision and inspiring guidance.

Prof. Valdas Pasiskevicius, for patient help and assistance operating the laser system.

Prof. Fredrik Laurell, for his entertaining leadership. He is in the most amusing way excellently leading a pleasant group towards result and performance.

Prof. Jens Tellefsen for kind practical help and useful input on energy distribution in focused beams

Hoon Jang who made my messy table look so tidy

Staffan Tjörnhammar, to whom I can direct and discuss any question at hand, regardless…

Alexander Agapow for brilliant help designing the laser trigging device

Michele Manzo for feedback and helpful discussions on circuit design

Dr Aman Russom for input toward an application of this work within Microfluidics, perhaps we will do something, sometime…

Finally to my wife, Maja, without her patience and unconditional support, studying at my phase in life would not have been possible.

Table of content

Introduction

1.1 Background

Material processing using lasers in society range from welding or cutting steel in the car industry, artistic decoration to cosmetic or invasive surgery. The success of using lasers in material processing depends on the high powers available and efficient light-matter interaction, combined with the ability to focus light onto a very small area or volume.

In microstructuring, or micromachining, the processing of the material is done at a micrometer scale. The major fields where microstructuring is employed are Microelectromechanical systems (MEMS), microfluidics, micro analysis (Lab-On-a-Chip or micro Total Analysis Systems)(LOC or µTAS) or structuring of transparent materials for photonics [1] . In all these fields, besides MEMS, glass is a good material because of its optical properties, chemical and thermal stability. Structuring of glass can be done by a range of lasers, the most common types are listed in Table 1.

Direct laser writing is a technique where the material to be processed is exposed to a focused laser beam and the material directly undergoes some desired change. Such a change can be material removal at the surface, void creation or change of material properties in the bulk. Traditionally, the limit for how small the structured feature can be is set by diffraction. Therefore, it is desirable to use as short wavelength as possible. However, to induce a change in the material, it needs to absorb photons at the processing laser wavelength. Silica based glasses, among other dielectrics, are transparent to visible light (VIS) and absorbs in the ultraviolet (UV) and near infrared (NIR) to infrared (IR).

Ultra short pulses in the context of material processing are in the range of one femtosecond to tens of picoseconds while short pulses have a typical duration of 10 ns. One major difference between ultra short and short pulse- to continuous-wave (CW) lasers is that due to the high peak intensity of ultra short pulses, non-linear processes are becoming significant under light-material interaction. Under such non-linear processes the material absorbs photons by multi-photon absorption. This means that the material only absorbs the light where the intensity reaches some critical level. This enables 3D structuring of, e.g., silica based glass, since the focus can be placed inside the material which is transparent to the irradiation up to some region close to focus where the intensity becomes critical.

Structuring of glass using ultra short pulses can be divided into two main processes; surface ablation for surface structuring and bulk structuring by locally changing the refractive index within the sample. By direct laser writing, these index changes can be used to inscribe wave guiding structures or, if periodically modulated, grating structures. Surface structuring can be used in the field of microfluidics to make channels with dimensions in the order of a few to tens of micrometers. With direct writing, high precision motion control and 3D structuring possibilities, microfluidic chip with complex geometries can be made. In glass chips, different wave guiding structures can be made in the same process giving a compact, complex chip with directly integrated sensing or analyzing capabilities. Further reading on microfluidic

systems and design can be found in references [2-9]. Structuring within the material, changing the refractive index, can be used for making miniaturized optical components [10], gratings in fiber [11] or bulk material [12, 13]. Those have a major importance in, i.e., tele-communication systems, laser design and spectroscopy.

Laser	Wavelength (nm)	Photon energy (eV)	Character
F_2 excimer laser	157	7.9	Pulsed
ArF excimer laser	193	6.4	Pulsed
KrF excimer laser	248	5.0	Pulsed
Nd:YAG Freq. Quadrupled	266	4.7	Pulsed
XeCl excimer laser	308	4.0	Pulsed
Nd:YAG Freq. trebled	355	3.5	Pulsed
Nd:YAG Freq. doubled	532	2.3	Pulsed
Ti:Sapphire	680-1,100	1.8-1.13	Ultra short pulse
Nd:YAG	1064	1.17	CW or pulsed
CO_2	10,600	0.117	CW or pulsed

Table 1 *Lasers commonly used for processing of glasses.* [1]

1.2 Project outline

The main purpose of this work was designing and building an experimental setup employing the high precision of the translation system together with a picosecond laser for microstructuring. Therefore the details regarding experiments and the more practical engineering of the system evolved as the project developed. During the first month of this work a literature study of direct laser writing in glass, and a survey of the technique for applications in microfluidics was made. Parallel to these activities, the specifications, precision and general behavior of the translation system and its programming language were studied. In addition, the concept of simulating a complex pattern by programming in Matlab® for use as input data for motion and position coordinates into the system was tested.

Following these activities, the system was designed in order to increase system flexibility (usability), improve precision, and reduce resonance effects of the translation stages. To

assemble and integrate the optics and translations stages, additional optical components were purchased while some components required special design and where made in-house. The mechanical system was then evaluated regarding the reproducibility and stability of the sample alignment.

After investigating different possibilities of position feedback-control from the hardware controlling the translation stages it was realized that an output signal could be generated relative to the coordinates of the translation stages. After characterizing this output signal a device was designed, having compatible interfaces between the sub-systems, that could trigger the laser based on the position coordinates of the translation system. The device was then assembled and implemented into the system successfully.

Evolution of the project work

Article study System behavior Laser trigging device Initial experiments
Programming System design System evaluation Experiment refinement
Matlab simulations System assembly Experimental design Final experiments

With the complete system assembled and aligned, using a HeNe laser reference beam, the stability of the setup was evaluated. The following step was to implement different experimental designs in order to test the system, followed by evaluation and subsequent adjustments and improvements. Once completed, experiments were performed for surface ablation studies followed by evaluation. Preliminary tests of bulk refractive index changes were also performed.

1.3 Thesis structure

After the introducing the concept of direct laser writing in ***Chapter 1***, the theory of interaction between light and glass will be described in ***Chapter 2***. Also bulk focusing complications will be mentioned upon. ***Chapter 3*** describes the different parts of the system and its assembly to a high precision laser processing system. Also synchronized computer controlled laser trigging and programming issues are described. In ***Chapter 4*** the experimental backgrounds and details are given. In ***Chapter 5*** the results are presented and discussed followed by conclusions and an outlook. ***Chapter 6*** includes the references used in this thesis followed by an ***Appendix*** containing material- and system- specific information, aligning procedures and supplementary images.

2 Light-material interaction

There are different degrees of modification that can occur with different underlying property change in the material. If no material interaction occurs the light is transmitted. If interaction does occur, different material modification seen in Table 2 can be induced.

Material property change	Modification	Physical mechanism
Defect formation	Increased index of refraction and absorption	Excited/trapped electronic states in matrix
Densification		Local change in bond structure
Extended modification	Smallest type of material removal or void forming in the bulk	Ruptured glass network
Void	void forming in the bulk	Melting, boiling and fracturing
Ablation	Material removal on the surface	Material ionization

Table 2 *Overview of material change, its underlying physical mechanism and the consequences.*

2.1 Absorption

In order for light to interact with the material, photons need to be absorbed by the material. Silica based glasses typically have a transmission window limited in the short wavelength region (typically 200-300 nm) by absorption of electronic origin, related to the optical band gap of the material or intrinsic defects. [14] The long wavelength limit (typically 2-3µm) is due to multi-phonon absorption of molecular dipole origin. Within these limits the material can be considered transparent. For long propagation distances, as in the case for long distance transmission in silica based optical fibers, losses to due to Rayleigh scattering become significant [11], as shown in Figure 1.

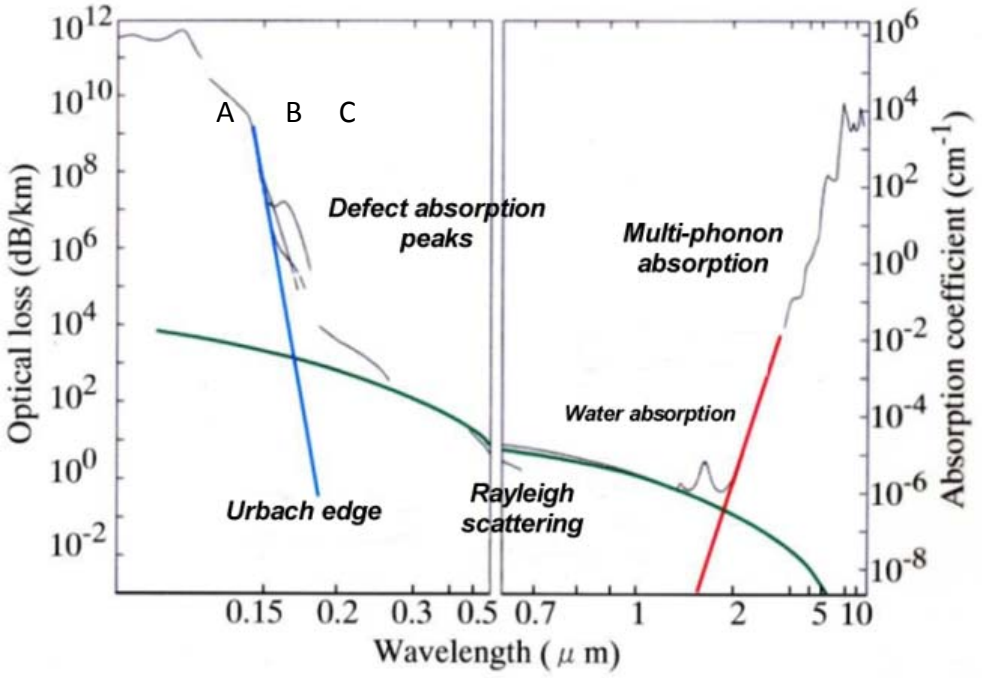

Figure 1 *Optical loss in optical fibers and the mechanisms behind the absorption.*

In glasses the absorption in the ultraviolet (UV) region, which is of main importance in laser processing, is characterized by three different regions (see Figure 1) the Tauc region (A), Urbach region (B) and defect or impurity related absorption (C). [14, 15, 16]

Tauc region

The absorption in the Tauc region is related to electronic transitions in high probability states (not contributing to band tails, see next paragraph, Urbach region). The optical bandgap, E_g, of a material is typically derived by extrapolating the absorption in the Tauc region to zero.

Urbach (tail) region

The disordered structure of the glass, which can be viewed as a non-perfect crystal structure, causes a broadened distribution of bond angles, primarily between SiO_2 units, leading to band tails. The Urbach energy is a measure of the width of the band tail, or disorder, in an amorphous dielectric.

Defects/impurity absorption

Defects and impurities can give rise to strong absorption bands typically located in the UV to VIS wavelength region. This absorption is directly linked to the structural and compositional properties of the material. A common defect is oxygen deficiency with an absorption band located in the UV region (λ ~190 - 250 nm). Absorption due to impurities is often related to transition metals ions with wide absorption bands extending from UV to VIS wavelengths.

Linear absorption regime – one photon absorption

For laser processing in the linear regime, the absorption coefficient of the material at the laser wavelength determines how local or extended the light-matter interaction will be. For weak absorption, the energy of the photons will therefore be absorbed over a longer distance, decreasing the amount of energy absorbed per unit volume. In this case, the low absorption may limit the ability to reach threshold for material modifications.

For very high absorption coefficients, most of the light will be absorbed at the surface layer where critical intensity is reached. Modification of the material will therefore be localized at the surface layer.

Nonlinear absorption regime – multi photon absorption

Multi photon absorption is the promotion of an electron to the conduction band by the simultaneous absorption of two or more photons, schematically shown in Figure 9. This process is less probable than single photon absorption and therefore requires high intensity laser beams being proportional to the laser intensity raised to the power of the number of absorbed photons in the process.

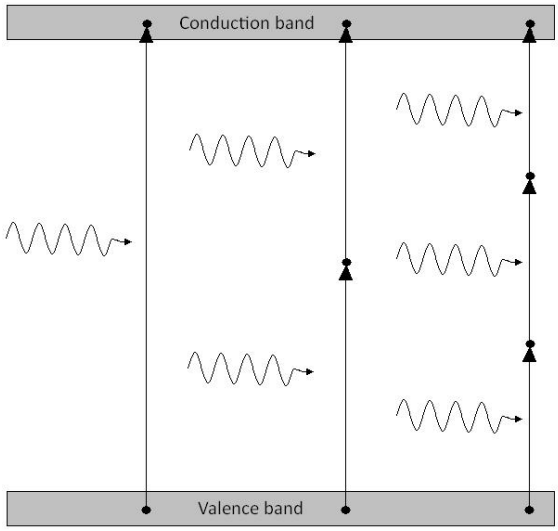

Figure 2 *Schematic of excitation to the conduction band by : One (ω), two (2ω) , three (3ω) photon absorption*

By focusing the light, increasing the intensity at the focal point, it is therefore possible to have a localized light-matter interaction within the bulk of the material as schematically shown in Figure 3. A consequence of multiphoton absorption is that 3D structuring is possible. Unfocused light (below threshold) will simply pass through the material without interaction. Figure 4 shows a numerical simulation of the intensity distribution when

focusing 800 nm light in vacuum down to a 5 µm beamwaist (black center area indicating volume above threshold)

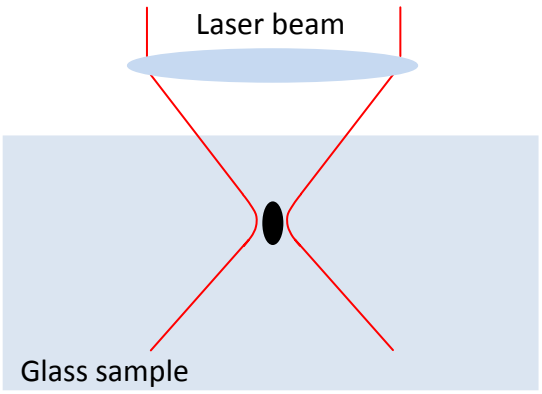

Figure 3 *Illustration of 3D structuring. The focus where critical intensity is reached placed inside a glass sample which is elsewhere transparent.*

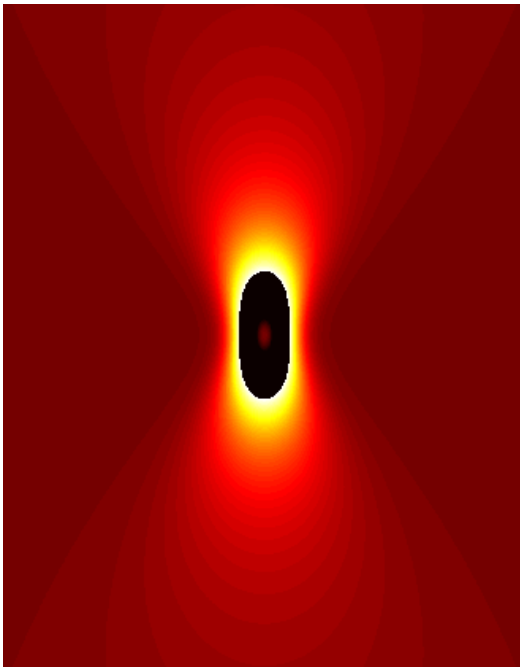

Figure 4 *Simulation of focusing in vacuum to illustrate the intensity gradient and shape of ablation region. The truncated (black) area indicates intensity above some critical level. The simulation for focusing is based on a beamwaist (ω_0) of 5 µm.*

In this thesis a commercial Boro-Aluminosilicate glass was used (Corning® EAGLE2000™) having an absorption spectra as shown in Figure 5. The corresponding wavelength for single- two- and three-photon absorption are also indicated in Figure 5, assuming a laser operating at a wavelength of 800 nm.

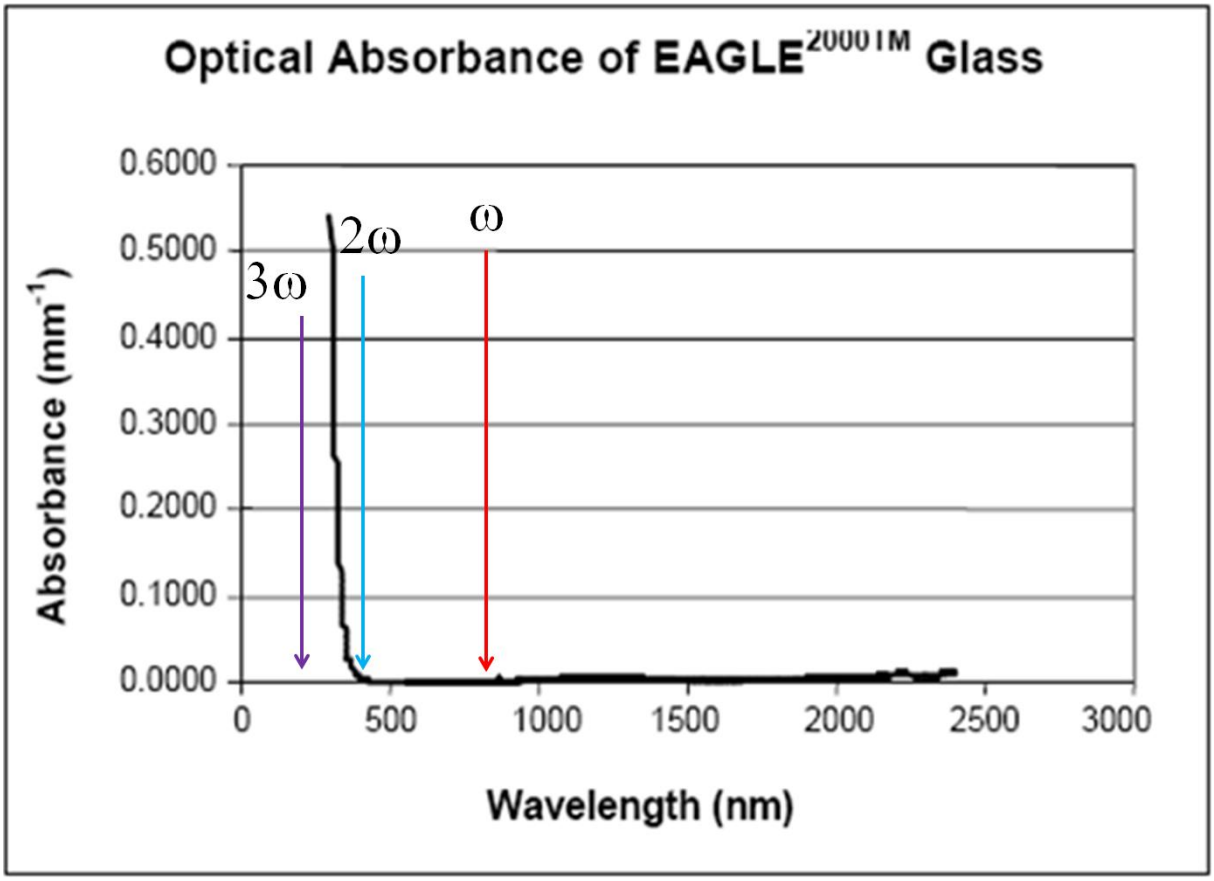

Figure 5 *Absorption spectra of Corning® EAGLE2000™ glass provided by the manufacturer and single- and multiple photon absorption indicated (λ=800nm)*

2.2 Thermal vs non-thermal

Thermal processes are typically associated with CW lasers or pulsed lasers with pulse durations above approximately $\tau \sim 100$ ps, while non-thermal processes are associated with lasers with pulse duration typically below $\tau \sim 10$ ps. For pulses shorter than $\tau \sim 10$ ps the energy deposit into the material occurs on a time scale that is shorter than the time required for heat to be transferred from the focal volume to the bulk of the material. In thermal processes the material is damaged due to heat accumulation resulting in melting, evaporation or fracturing of the material. [17] Non-thermal processing does not induce a thermal build-up, provided the repetition rate is below critical value [13], but changes the bond structure in the material.

On the surface this can result in material removal by cold ablation, while in the bulk it may result in material densification or damage (void formation). In the thermal regime the damage threshold typically scales as the square root of pulse duration, $\sqrt{\tau}$ [18]. In the non-thermal regime most research [19] indicates a linear τ dependency.

2.3 Interaction mechanisms for short pulses

There are generally two different processes that occurs when a laser pulse with a duration from a few femotoseconds to the order of tens of picoseconds is focused into a glass sample; *Photo ionization* and *Avalanche ionization* [20]

Photo ionization

Photo ionization is divided into two possible processes; *tunneling ionization* and *multiphoton ionization*. In the case of tunneling ionization the electromagnetic field of the laser pulse suppresses the Coulomb attraction between the electron and nucleus (i.e. the Coulomb well holding the electron) which reduces the potential so that the electron is exited to the conduction band or ionized. For multiphoton ionization, the ionization rate is given by $P(I) = \sigma_k I^k$ where I is the laser intensity, σ_k is the multiphoton absorption coefficient, and k is the number of photons required to reach the optical bandgap, E_g ($k\hbar\omega \geq E_g$, $\hbar\omega$ = photon energy). For tunneling ionization, the rate scales somewhat weaker with the laser intensity. Although the effects are very similar, the concept and calculations are very different. An indication of which process is occurring is often given by the adiabatic, or Keldysh, parameter (γ) given by: [21]

$$\gamma = \frac{\omega}{e}\sqrt{\frac{mcn\varepsilon_0 E_g}{I}}, \qquad (3.1)$$

where I is the laser intensity at focus, ω is the laser angular frequency, c is the speed of light, m is the reduced electron mass, e is the electron charge, n is the refractive index, and E_g the optical bandgap, ε_0 is the permeability of free space. In Figure 6 the ionization mechanisms, with corresponding Keldysh parameter, are illustrated. For a Keldysh parameter of approximately $\gamma \approx 1.5$ the photoionization is a combination of tunnelling- and multiphoton ionization. For $\gamma > 1.5$, multiphoton ionization dominates while below, $\gamma < 1.5$, tunnelling ionization is the dominating process.

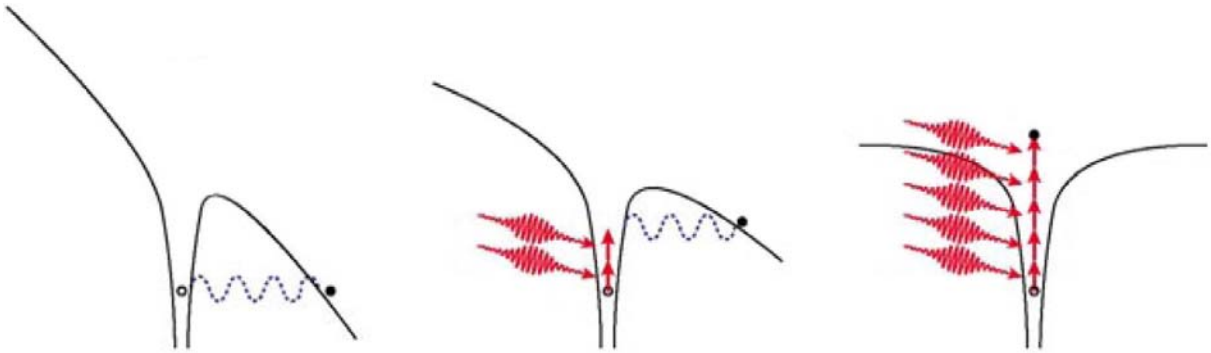

Figure 6 *Photo ionization mechanism given by the adiabatic, or Keldysh parameter. (Illustration taken from ref. .[20]*)

Avalanche ionization

For laser pulses with a duration of $\tau > 100$ fs, avalanche ionization is reported to be the main interaction process. [17] Avalanche ionization depends on *seed* electrons and for relatively long pulses (1 ps < τ < 10 ps) the seed electrons are provided by either thermal excitation or by excitation of material inherent impuries. As the pulse duration decreases (τ < 1 ps), seeding electrons are increasingly supplied through multi-photon ionization generated by the leading edge of the laser pulse. As a consequence the avalanche process becomes less dependent on stochastic material-inherent seed electrons and hence more deterministic. Whether pulse durations below 100 fs is an approximate limit for which multiphoton ionization becomes dominant is still under debate. [22]

Avalanche ionization is a process of multiple steps starting with photons absorbed by free carriers, i.e. seed electrons. The number of absorbed photons, k, is given by $k\hbar\omega \geq E_g$ and the excessive energy goes into kinetic energy, allowing the ionized electron to collide and by impact ionization promotes a valence band electron to the conduction band, i.e. generating free carriers. The electron density, N, grows when the laser pulse is present according to,

$$\frac{dN}{dt} = \eta N \,, \qquad (3.2)$$

where η is the avalanche ionization rate. Although the intensity dependence of the avalanche ionization rate, η, is under discussion, recent reports suggest a linear dependence, $\eta = \alpha I$, where α is the avalanche coefficient. [23]

Since avalanche ionization starts with free carrier absorption, the generation of free carriers is more relevant to the non linear absorption. The free carrier generation rate is then given by,

$$\frac{dN}{dt} = P(I) + \eta N \,, \tag{3.3}$$

where $P(I)$ is the photo ionization rate. The number density of free carriers relates to the plasma frequency as,

$$\omega_{pe} = \sqrt{\frac{4\pi n_e e^2}{m^*}}, \tag{3.4}$$

where n_e is the number density of free carriers, e is the electric charge, m^* is the effective mass of the electron, and ε_0 is the permittivity of free space. As the number density of electron grows by avalanche ionization, a high-density plasma is formed. This plasma strongly absorbs the laser energy by free-carrier absorption. The plasma becomes reflecting when it reaches the laser frequency. However, up to this critical level, sufficient energy is absorbed to generate material damage or modification. For pulses with a duration in the non-thermal regime, this energy is transferred into the surrounding atomic structure of the material after the pulse is gone and no accumulation of heat occurs.

2.4 Ablation, densification and incubation effects

For pulse energies below ablation threshold on the surface or damage threshold in the bulk a structural change in the material may occur that leads to an increase in the index of refraction as a result of material densification. In this work the main concern was ablation so no thorough investigation of wave guiding structures or gratings was done.

In the region where a structural change has been induced there is also an incubation of the material in the sense that the threshold for material interaction is lowered. During material processing, thermal effects from successive laser pulse interactions may also affect the threshold. In this work, the change in ablation threshold under multi shot exposure was found to be different when the repetition rate was 1kHz as compared to manually triggered shots at about 1 Hz. This is probably explained by thermal effects. The thermally affected region outside ablated area provides an increased number of seed electrons, i.e. thermally exited electrons, for the avalanche ionization process. Since this is a very efficient process [20, 28] the ablation threshold should be affected even by a minor increase in seed electrons. Another result of elevated temperature is a weakening in the material.

Under translation and at some laser pulse repetition rate the effective number of overlapping pulses are given by $N_{effective} = \frac{D \cdot f}{v}$ where D is the $1/e^2$ spot diameter, $2 \cdot \omega_0$, f is the pulse repetition rate and v is the translation speed. As the material is incubated from

successive partially overlapping pulses, these effects are accumulated in the material which results in an expansion of the incubated region. In Figure 7 a simulation of the energy density in a Gaussian beam is simulated. A region of some damage threshold is truncated and the intensity gradient can be seen outside this region.

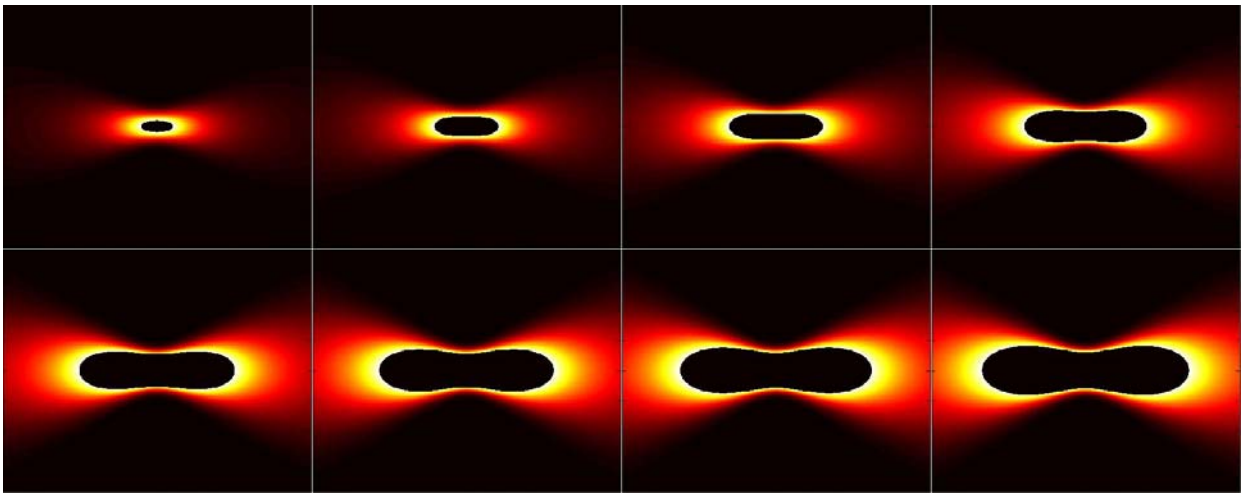

Figure 7 *Simulation of intensity distribution in a focused, Gaussian, beam and with intensity above threshold marked. Illustrative image with ω_0= 5µm. The images are side views of the sagital plane of the focused beam.*

2.5 Bulk focusing complications

Complications with bulk focusing are mainly self focusing due to high peak power and spherical aberrations.[20] The self focusing is more significant at low numerical aperture (NA) objectives (NA < 0.5) since the energy gradient is smaller while aberrations becomes more pronounced at high NA (NA > 0.65) since the paraxial approximation is not valid. By ray tracing it can be shown that there are optimal focusing depths depending on the refractive index of the material where the spread of rays are below 100nm and aberrations can be neglected. Provided aberrations can be neglected, the major problem is self focusing which makes it hard to accurately determine the laser intensity at the interaction site. This makes bulk damage thresholds or thru sample ablation thresholds problematic to determine. In ref [20] there is a more comprehensive review of bulk focusing issues.

3 Laser processing system

The system is an integration of several sub-systems, see Figure 8, to an assembly of high precision translation stages, delivery of ultra-short laser pulses for direct writing and a reference beam for precision alignment. The mechanics was set up to reduce vibrations and resonances in the system and a high precision adjustable sample holder was made. In Figure 9 a schematic of the assembled system and beam delivery is shown. The beam is focused by a 20X microscope objective, NA 0.5, giving a theoretical spot size of 1 µm ($1/e^2$ diameter).

Also on-line monitoring for direct evaluation and a device for computer controlled laser firing are implemented.

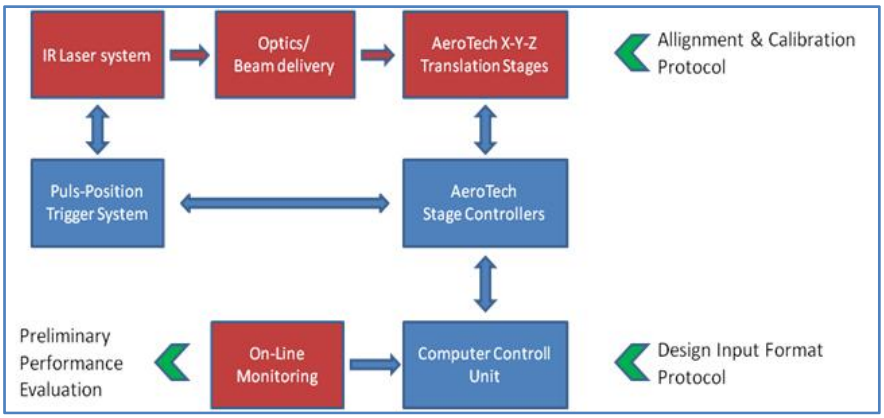

Figure 8 *Diagram of experimental set-up and the integration of different sub-systems*

3.1 Laser system

The laser system in short is a Ti:Sapphire femtosecond laser that seeds an amplifier which delivers pulses with a duration of approximately 1 ps at a repetition rate of 1 kHz. The spectral bandwidth at FWHM is approximately 10 nm centered at 800 nm and the maximum pulse energy is approximately 850 µJ. Previous M^2 measurements gave a value of approximately 1.5.

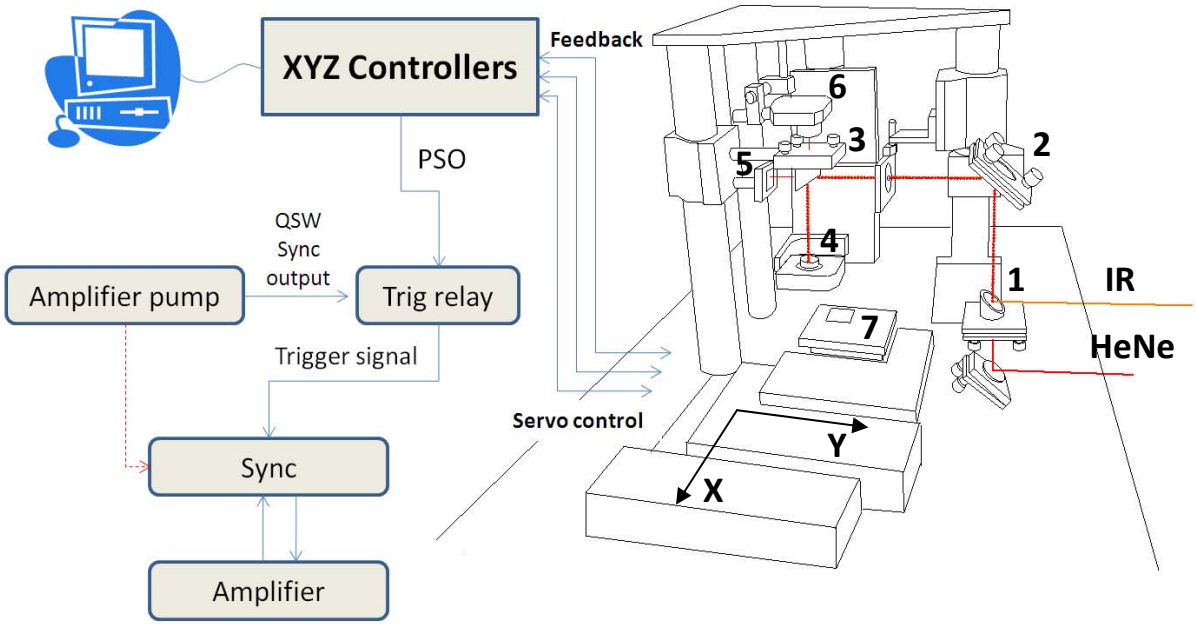

Figure 9 *System overview; Computer, controllers, laser trigging and laser writing setup. The dotted red line is the QSW sync output when a trigger signal relay is not used.* ***1)*** *Dichroic mirror HR@800nm HT@633nm* ***2)*** *Aluminum mirror* ***3)*** *Beamsplitter R/T 30/70 % @633nm and HR @800nm* ***4)*** *Microscope objective, achromat 20X NA 0.5* ***5)*** *Glass, same as sample* ***6)*** *CMOS Camera (Thorlabs DCC1545M)* ***7)*** *Adjustable sample holder*

3.2 Translation system

The translation stages are Aerotech ALS130H with a range of translation of 50 mm in X- and Y-direction (in the plane) and 25 mm in vertical Z-direction. Ideally the resolution is 4 nm and the repeatability is 100 nm in each direction. The real precision is maximized by identifying resonances in the setup and optimizing feedback parameters. See appendix 7.4 for further details.

The DC servo motors in the stages are controlled by the Ensemble 10MXU controllers. When the motion has been programmed the Ensemble software compiles and transfers it to the controllers. The motion is then executed non-interactively. The Ensemble controllers have position synchronized output, PSO, which can be programmed to generate an output signal relative to the position of the translation stages. The signal has the same accuracy as the position since the output is based on position feedback.

3.3 Computer controlled laser trigger

The PSO output signal from the servo motor controllers is a square wave where frequency and pulse width is defined in the script. This can be used for trigging the laser at certain positions or over certain intervals. The laser amplifiers pump has a pulse repetition rate, Q-switch sync, which is synchronized with the femtosecond laser source. In order to trig a single or a train of pulses, the clock frequency of the enable signal from the Ensemble controllers has to be exactly the same as the frequency of the amplifier pump. Since accuracy down to the computer number precision is not enough it was not possible to use the computer clock frequency. Therefore, a device which uses the frequency of the amplifiers pump laser as a reference signal was made, principle of operation shown in Figure 10. This device generates compatible trigger pulses at the frequency given by the reference frequency from the amplifiers pump laser. The signal from the controller is used as an enable signal and still with the ability of trigging a single laser pulse. The schematic for the device is given in the appendix, 7.2.

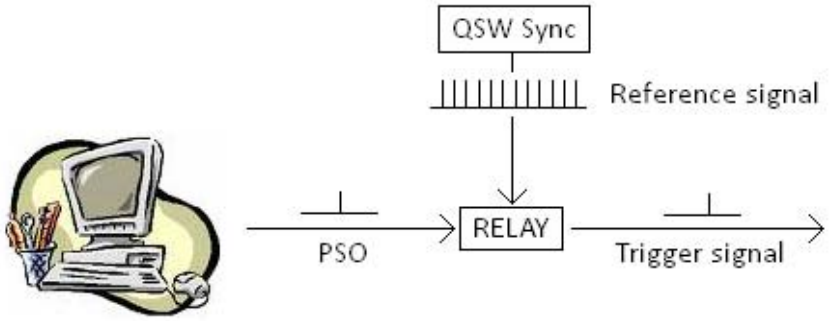

Figure 10 *Principle of relay for pulse enable signal*

3.4 Programming and motion design

The Ensemble software supplied by Aerotech resemble Visual Basic and has functions for commanding basic motion, retrieving feedback and status, enabling position synchronized output, PSO, etc. The enabling of PSO is programmed in the script that also commands the motion which gives the ability to turn the output on and off at specific positions and over certain intervals.

When a more complex pattern was to be generated it was found easiest to model the pattern in Matlab® and export coordinates which then can be used with various interpolation commands in the Ensemble software. It is also possible to parse a .dxf CAD file which gives a very convenient way to draw the pattern in a CAD program and import the coordinates for interpolation. Different interfaces were made for modeling a pattern, for example a spiral, see Figure 11, which is complicated to program in the Ensemble IDE.

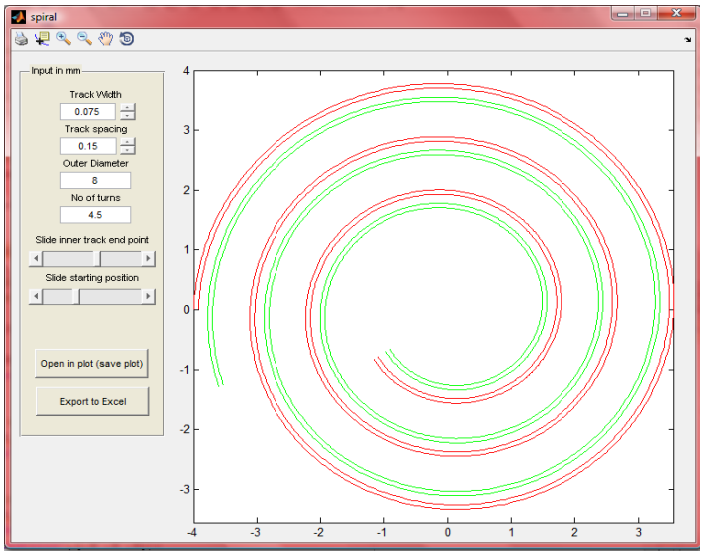

Figure 11 *Interface made in Matlab® to generate a spiral track and coordinates for export to the Ensemble software for interpolation.*

Also a module that generates coordinates for point vice laser shots from an imported picture was made (Figure 12). The image is discretesized at a certain threshold and size and resolution is defined.

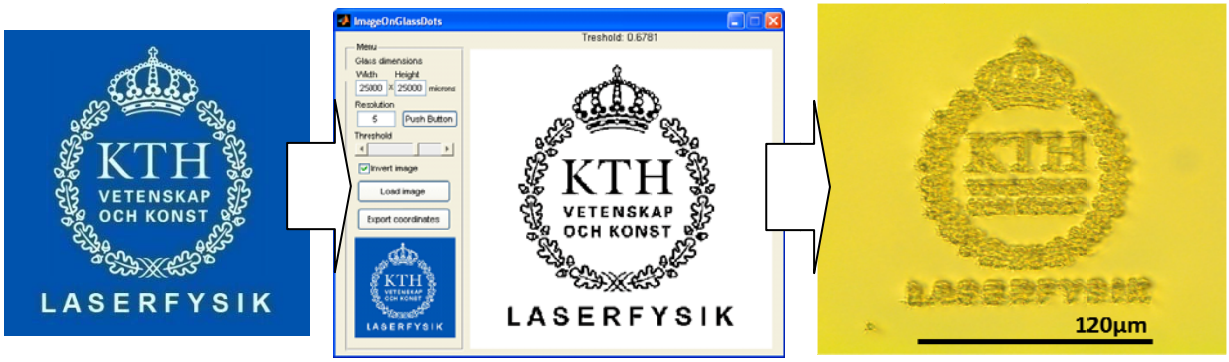

Figure 12 *Using the image import interface made in Matlab® to generate coordinates for point wise laser firing.*

3.5 Online monitoring and alignment procedure

In order to get a better overview and a means of faster evaluation a microscope was implemented in the sense that a transmitting (Koehler) lightning system was made, making it possible to use the camera for imaging the sample at the magnification of the microscope objective. The lightning system is not shown in Figure 9 but is guided in by a tilted mirror under the sample. An alignment procedure was worked out starting by interferometrically aligning the sample in the XY translation plane with an accuracy of +/- 100nm. The full alignment protocol is given in appendix 7.1.

4 Experimental methods

To test system performance a series of experiments were carried out to evaluate precision of the translation stages, computer controlled laser trigging and the software described in section 3.4. Also preliminary tests for drilling micro holes and writing high aspect ratio surface structures were done.

Threshold energies for ablation were investigated for top- and bottom side ablation. These thresholds give a quantitative basis for the parameters translation speed i.e. effective pulse overlap and pulse energy.

Surface structures were made by ablation at the top- and bottom side of glass samples. Bottom side writing can suffer from focusing problems while top side writing has problems resulting in poor agreement to input design. These are accumulation of debris within the structure and refocusing but primarily distortion, shadowing and diffraction of the laser beam. Also ablation of high aspect ratio structures was done.

The glass, Corning® EAGLE2000™, is an Alkaline Earth Boro-Aluminosilicate glass primarily used as substrate for Active Matrix flat panel displays. This glass has an absorption peak in UV and is transparent in the visible (VIS) to NIR region. The sample is 25x25 mm and 1.1 mm thick. It is thermally, temporally and chemically stable. It has low conductivity and cost.

All experiments were done by direct focusing in air at atmospheric pressure and when referring to pulse energy or fluence at the sample, losses in the objective were neglected. All glass samples were cleaned in a process of 3 x 5 minutes in ultra sonic bath with Touloen, Acetone and deionized water, respectively.

4.1 Testing the system

To test the system's ability to trig laser pulses commanded in the script along with the motion and to generate coordinates from complex geometries, two tests were done. First a script was written in the Ensemble IDE to make incremental steps of 5 µm and at each stop fire a single laser pulse at the sample surface. Secondly the Matlab® program described in section 3.4 was used to import a complex geometry from an image file to generate coordinates. With decreasing separation between the coordinates, a number of runs were done with iteratively adjusted pulse energies and number of overlapping pulses. Focus was placed inside the sample 170 µm below the surface. The result was analyzed by inspection using an optical microscope. In the second test the result is determined to be resolvable or not. This is rather subjective but lacks a more objective approach.

The pulse energy in the first test was 12 µJ. In the iterative process of the second test the initial pulse energy was 18 µJ and the number of overlapping pulses 15. The energy was reduced in steps of 2 µJ down to 2 µJ and the reduction in coordinate separation in steps of 0.2 µm from 2 µm down to 0.4 µm. As energy was reduced with decreasing separation the

range of tested number of pulses was lowered down to 2 overlapping pulses for the smallest separation.

Drilling

Drilling of micro holes through the sample was investigated. To avoid scattering, refocusing or other complications discussed in the top side writing section, the focus was places under the sample and the drilling was done starting from the bottom side. The sample was investigated by inspection using an optical microscope. By observing if water goes thru the micro hole by capillary forces, it would be shown that the drilled hole is void and without obstacles. The pulse energy was increased from 10µJ up to 60µJ in steps of approximately 5µJ. The translation speed, i.e. effective number of pulses was decreased from 3mm/s down to 0.6 mm/s in steps of 0.2 mm/s.

High aspect ratio surface structures

To investigate capability of making high aspect structures on the bottom side, tracks designed to have a 10x40 µm cross section was written. The pulse energy was chosen rather high to assure ablation at moderate translation speed and to make tracks wider than the beamwaist diameter by initially placing focus below the sample, see Figure 13. After cutting the sample it was cleaned in 2x7 min in toluene and acetone and rinsed in deionized water. The sample was then investigated by inspection using an optical microscope.

Parameter	Range
E_P – Pulse energy	44 µJ
Translation speed	1.2 mm/s
ΔX	20 µm
ΔZ	6X6 µm

Table 3 *Parameters for writing high aspect ratio structures. The move in X-direction is long enough to make parallel tracks, i.e. only one sweep per Z-layer and track.*

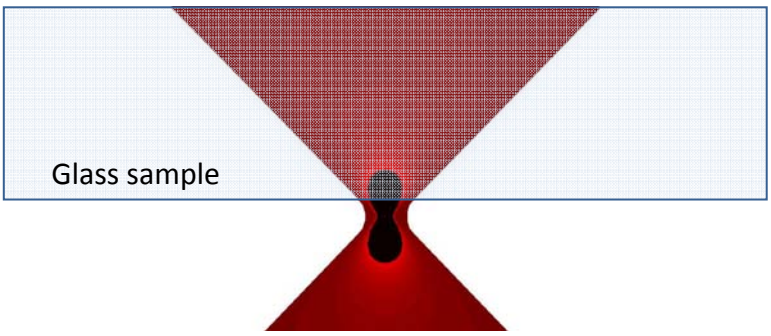

Figure 13 *High energy beam focused thru the sample with the beamwaist approximately 10 µm outside the sample. The black region indicates area with fluence above ablation threshold. Above, outside, this illustration the beam is focused thru the objective, the thickness of the sample or the beam is not to scale. The beam illustrates a Gaussian beam focused in vacuum, no absorption in the sample is included in the model and no bulk focusing complications are taken into account.*

4.2 Determining threshold for ablation

In literature reported ablation parameters such as energy threshold and absorption coefficient vary between groups. Experimental results are likely to vary depending on beam delivery and focusing and between laser systems [22, 23]. The most commonly used method, initially proposed by J.M Liu [24], is based on measuring and profiling the crater resulting from ablation at the surface. The diameter of the crater, D, is measured for different pulse energies or in other terms the average fluence F_0^{av}. A linear relation between the square of the diameter D^2 and the logarithm of the average fluence $\ln(F_0^{av})$ is derived and measurements of D for different pulse energies are fitted and extrapolated to $D^2 = 0$ which gives the threshold fluence. The derivation starts from the fluence for a Gaussian beam,

$$F(r) = F_0^{peak} exp\left(-\frac{2r^2}{\omega_0^2}\right), \tag{4.1}$$

where F_0^{peak} is the peak fluence in the centre of the Gaussian beam, ω_0 is the $1/e^2$ radius and r is the radial coordinate. Putting r=D/2 and arguing that the fluence threshold, F_{th}, is the peak fluence for which the diameter of the ablated crater is zero. This gives:

$$D^2 = 2\,\omega_0^2 ln\left(\frac{F_0^{peak}}{F_{th}}\right) \tag{4.2}$$

The peak fluence is related to the pulse energy as,

$$F_0^{peak} = \left(\frac{2\,E_{pulse}}{\pi\omega_0^2}\right) \tag{4.3}$$

For the sake of being consistent with literature and to get the ablation threshold in terms of pulse energy F_0^{av} which is the average fluence is used. The average fluence relates to pulse energy as,

$$F_0^{av} = \left(\frac{E_{pulse}}{\pi\omega_0^2}\right) \tag{4.4}$$

Using F_0^{av} instead do not change the slope of Eq. 4.1 and the relation becomes,

$$D^2 = 2\,\omega_0^2 ln\left(\frac{F_0^{av}}{F_{th}}\right) \tag{4.5}$$

Experimentally it is more convenient to measure pulse energy so the ratio between fluence in Eq. 4.4 is replaced with the ratio between pulse energies,

$$D^2 = 2\,\omega_0^2 ln\left(\frac{E_{pulse}}{E_{th}}\right) \tag{4.6}$$

When the threshold energy has been determined for single shots, Eq. 4.5 also provides a way of experimentally calculate the spot size, assuming a Gaussian beam.

There are other similar approaches [25] using ablated volume and no discrimination between single- and multi shot ablation.

Matrixes with ablated craters were made at the bottom of the sample for a range of pulse energies and number of pulses. Multiple pulse shots were fired at the laser's repetition rate, 1 kHz. The distance between laser shots was 50 µm which is considered to be enough to leave the material unaffected by neighboring shots. The relative distance between beamwaist and surface was changed in steps of 1 µm to find optimal position.

The samples were analyzed by measuring the diameter of ablated craters using an optical microscope, obtaining threshold energy using Eq. 4.5. The optimal position of the beamwaist was taken as that for which the ablated craters were most symmetrical with minimal cracks around the edge.

The error in measuring ablated craters origins from cracks resulting in an uncertainty up to 15%. For low pulse energies and low number of shots it was not possible to get useful data from bottom side written matrixes. The pulse energies ranged from 13 µJ to 34 µJ and the number of shots from 30 to 60.

4.3 Top- vs bottom side ablation

When ablating material from material top surfaces, problems with beam distortion, refocusing etc can occur. These problems can be related to residual debris scattering or partially blocking the beam but could be avoided by writing structures on the bottom side by focusing thru the sample. Using this approach the beam is not disturbed by residual debris and it propagates in a homogeneous material up to the interaction site.

Using the same motion design, straight tracks were ablated on the top- and bottom side. The programming was done so that a quadratic cross section of 40X40µm would be made. Approximating the ablated region to expand 5 µm radially from the focal point, the motion was stepped 6µm laterally and in depth. All tracks were straight, 2mm long so that the sample could be cut and polished. The cross sections of the cut sample were analyzed by inspection using an optical microscope. The top view was inspected to estimate the edge roughness. The parameters for channel ablation are given in Table 4.

Parameter	Range
E_P – Pulse energy	*10-65 µJ*
Translation speed	*0.2-2.6 mm/s*
ΔX	*6 µm*
ΔZ	*6 µm*

Table 4 *Parameters for top- and bottom side writing of straight tracks. The tracks was designed to have a 40x40 µm cross section so the move in X and Z directions were made six times.*

5 Experimental results

5.1 Testing the system

A row of ablated craters with a diameter of 5µm was written on the top side of the sample. A major part of the shots are positioned correctly but some shots appear to have a position error within 1 µm, see Figure 14. This is probably explained by a non-uniform crater as a result of a stochastic behavior of the light-material interaction, partially because of incubation effects from neighboring shots and partially because of intrinsic material defects which have a higher impact in the picosecond regime as compared to femtosecond pulses.

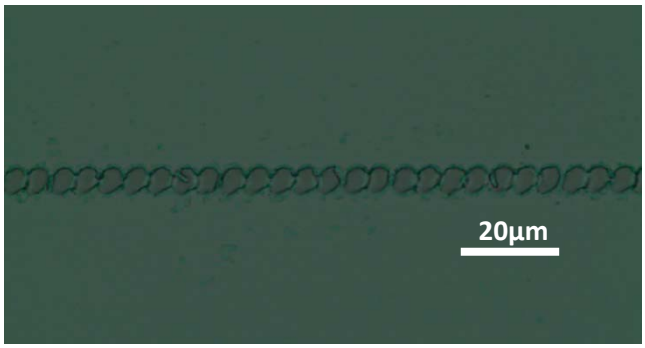

Figure 14 *Row of point-wise fired laser shots, pulse energy 12µJ, incremental movement of 5µm.*

In Figure 15 two images made by point vice shots are shown. The smallest pixel separation for a picture assessed as just resolvable (Figure 15 B) was 0.6 µm, the pulse energy was 3µJ and 4 overlapping shots. In the left picture the separation is 0.9 µm, pulse energy 5 µJ and 6 overlapping shots. The right picture was not possible to image using the optical microscope. The image is acquired using the systems integrated microscope.

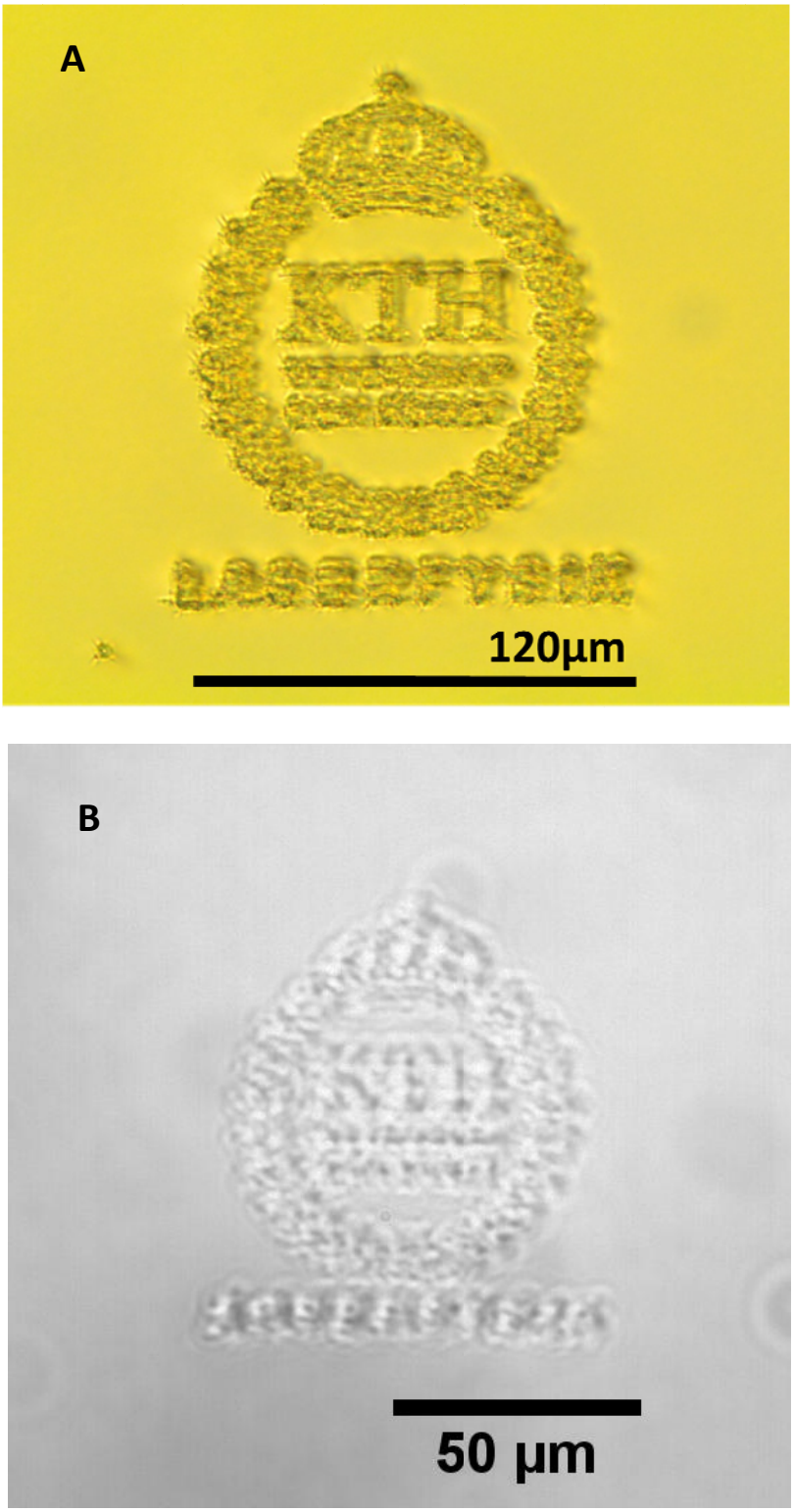

Figure 15 *Single pulse trigging at coordinates generated with a Matlab® program that discretizises an image and generates coordinates based on sample size and resolution i.e. distance between two pixels not separated in the original image. A: Coordinates where pulses are triggered are separated 0.9 µm, pulse energy 5 µJ, 6 overlapping pulses. B: Separation 0.6 µm, pulse energy 3 µJ, 4 overlapping pulses.*

Drilling

In Figure 16 the best result of micro hole drilling is shown. The pulse energy was 35µJ and the translation speed 0.8mm/s for the left hole to 1.8mm/s for the right in steps of 0.2mm/s. Focusing thru the sample at the bottom, the rightmost spot showed potential to be a genuine thru-sample hole. To find evidence for a hole thru the sample without obstacles, it was tried to show a capillary water flow. This could not be seen which could imply that grains are accumulated in the hole or that the capillary water flow is hard to detect.

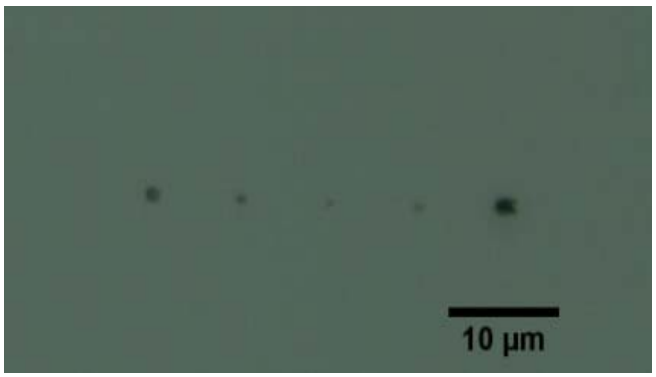

A

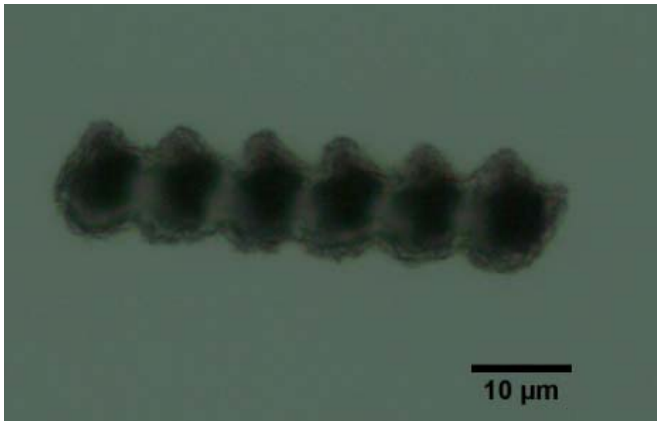

B

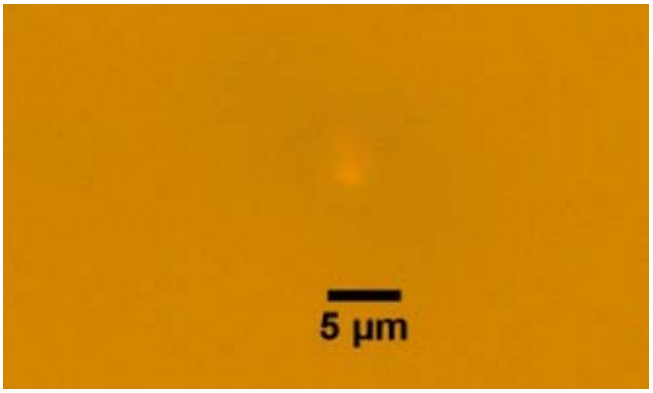

C

Figure 16 *Array of structure written thru sample, in the Z direction. A) Bottom side B) Top side C) Focusing on the rightmost spot in B thru the sample on the bottom with transmitted light (EPI)*

High aspect ratio surface structures

Straight tracks with an aspect ratio of 1:3, approximately 8µm wide and 30µm deep was written on the sample bottom side, see Figure 17.

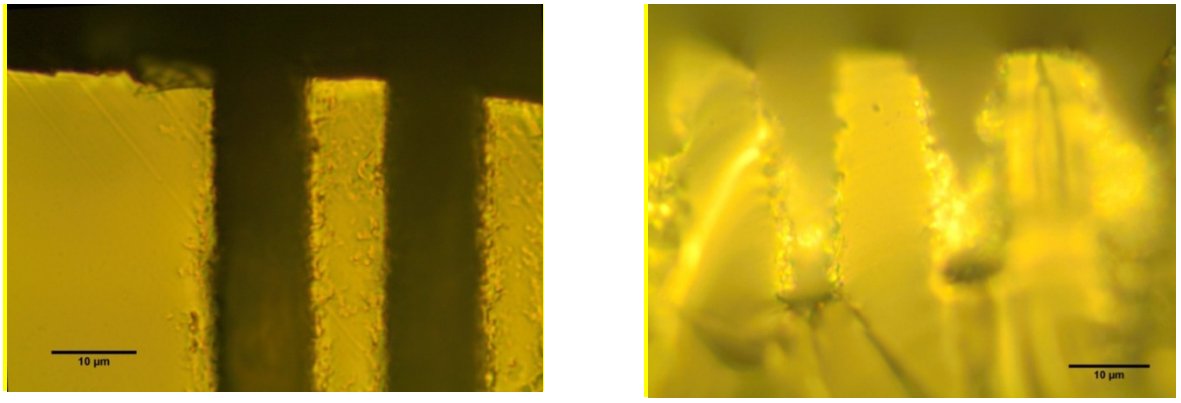

Figure 17 *Top side view and section of high aspect ratio structures.*

The ablation of material occurs in the part of the beam where it converges but the energy density is still above ablation threshold.

The reason for choosing high pulse energy (44 µJ) is to enhance debris removal from the tight structure by removing the full width in one over run per layer. As seen in the sectional image (Figure 17) there seems to be some material left in the structure. This is probably due to choice of pulse energy and translation speed and not to problems with material or debris removal. Lower pulse energy and lower translation speed would probably be a better choice, perhaps with multiple sweeps.

5.2 Determining threshold for ablation

Threshold pulse energies for ablation for focusing thru sample are given in Table 5. For focusing on the top side and for 10 overlapping pulses, the threshold pulse energy was determined to 10.1 µJ. A typical matrix is shown in Figure 18 and the fit of ablated crater diameters in Figures 19 and 20.

Number of pulses	Pulse energy ablation threshold [µJ]
30	18.8
40	16.1
50	14.1
60	12.0

Table 5 *Obtained pulse energy thresholds for material ablation using 1 ps pulses. The beam was focused with a 20X 0.50 NA microscope objective thru the 1.1 mm thick sample.*

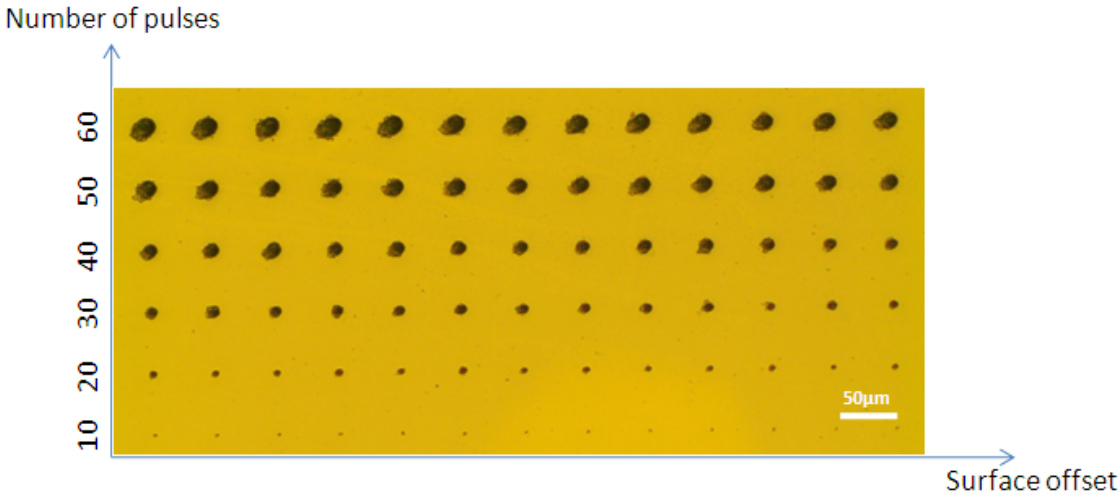

Figure 18 *Matrix of craters ablated on the bottom side of the sample. The crater diameters were measured using an optical microscope and fitted according to eq. 4.6 to give threshold energy for ablation.*

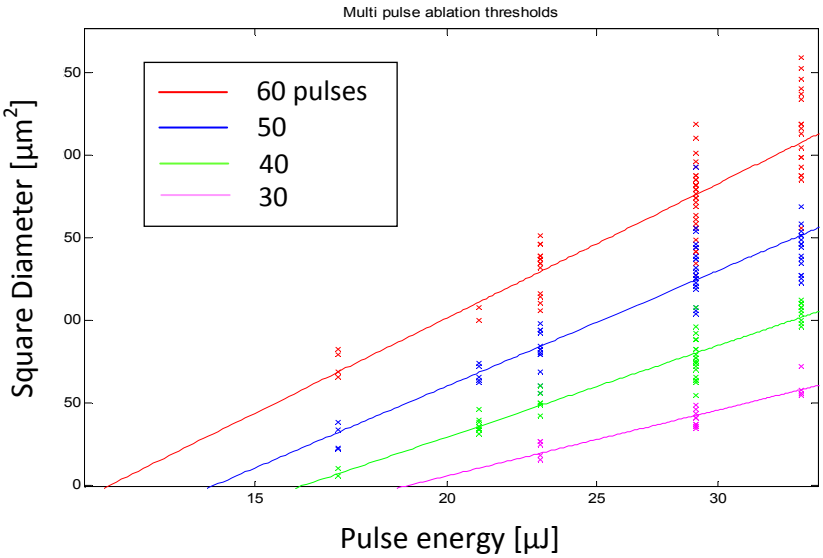

Figure 19 *Plot of fitted data for obtaining bottom side ablation thresholds. Threshold energies are given in Table 5.*

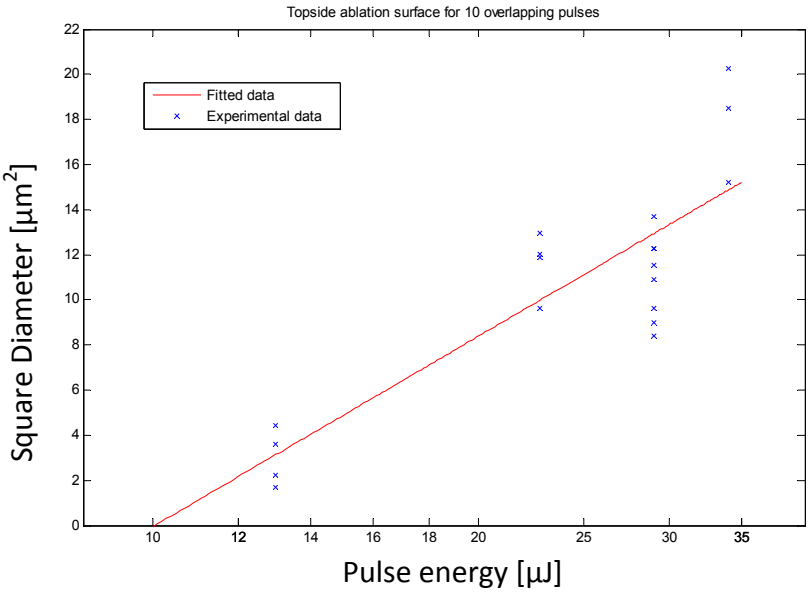

Figure 20 *Fit of data from top side ablated matrix with 10 overlapping pulses. Threshold pulse energy is 10.1µJ.*

5.3 Top- vs bottom side ablation

Top side writing

In Figure 21 the cross section of a topside written track is shown. Writing tracks on the topside resulted in the same profile for the range of parameters given in Table 4, at least as could be determined under inspection using an optical microscope.

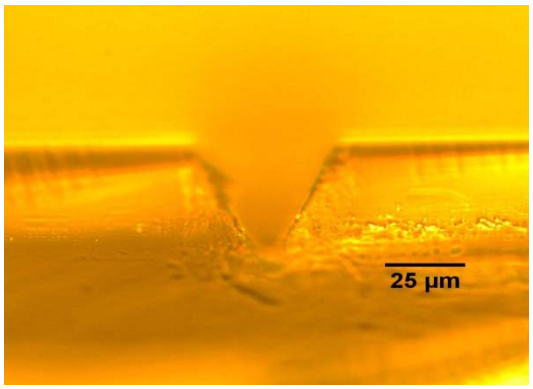

Figure 21 *Cross section of topside written track designed to have a square cross section of 40x40 µm, pulse energy 20 µJ , translation speed 1.2 mm/s*

Bottom side writing

In Figure 22 tracks written on the bottom side is shown. It is found that the result is highly dependent on pulse energy and translation speed, i.e. effective pulse overlap. The shape of the cross section (curvature and width) seems to be related to the intensity gradient and consequently the result of incubation effects. In Figure 24 a scatter plot of deviations from design input is given. With correctly chosen input parameters the shape of the cross section can be controlled regarding depth, width and bottom curvature. The result of excessive pulse energy is seen in Figure 23. The intensity grows critical within the sample, changing the material so that the beam is scattered or refocused, which results in uncontrolled damage. In appendix 7.5, a larger set of cross section images is given.

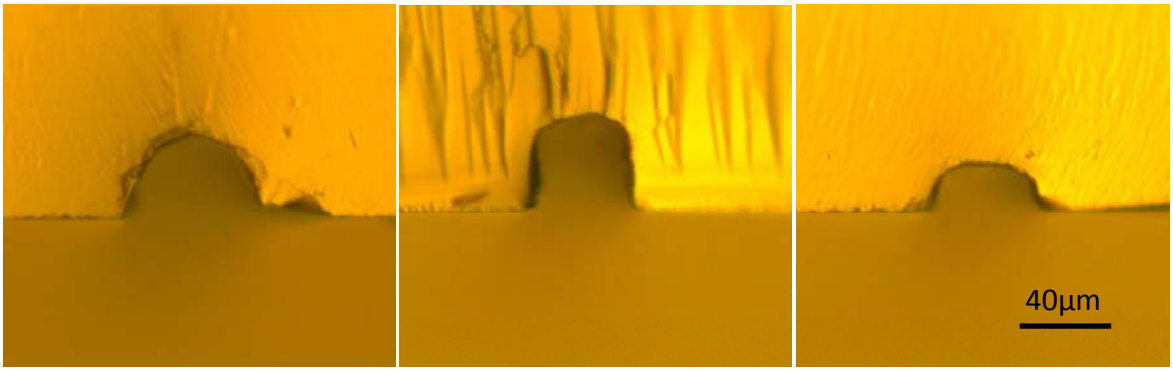

(a) (b) (c)

Figure 22 *Cross sections of tracks written with; a: High pulse energy, high translation speed b: Moderate pulse energy, moderate translation speed c: Low pulse energy, high translation speed*.

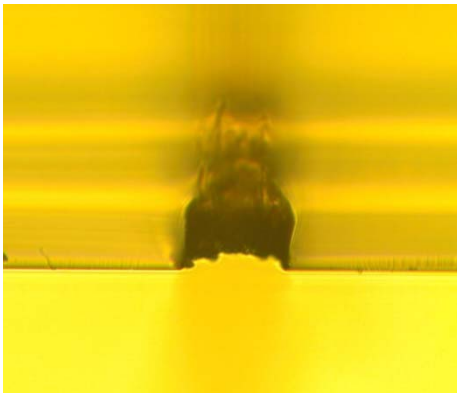

Figure 23 *Uncontrolled damage as a result of excessive pulse energy and low translation speed.*

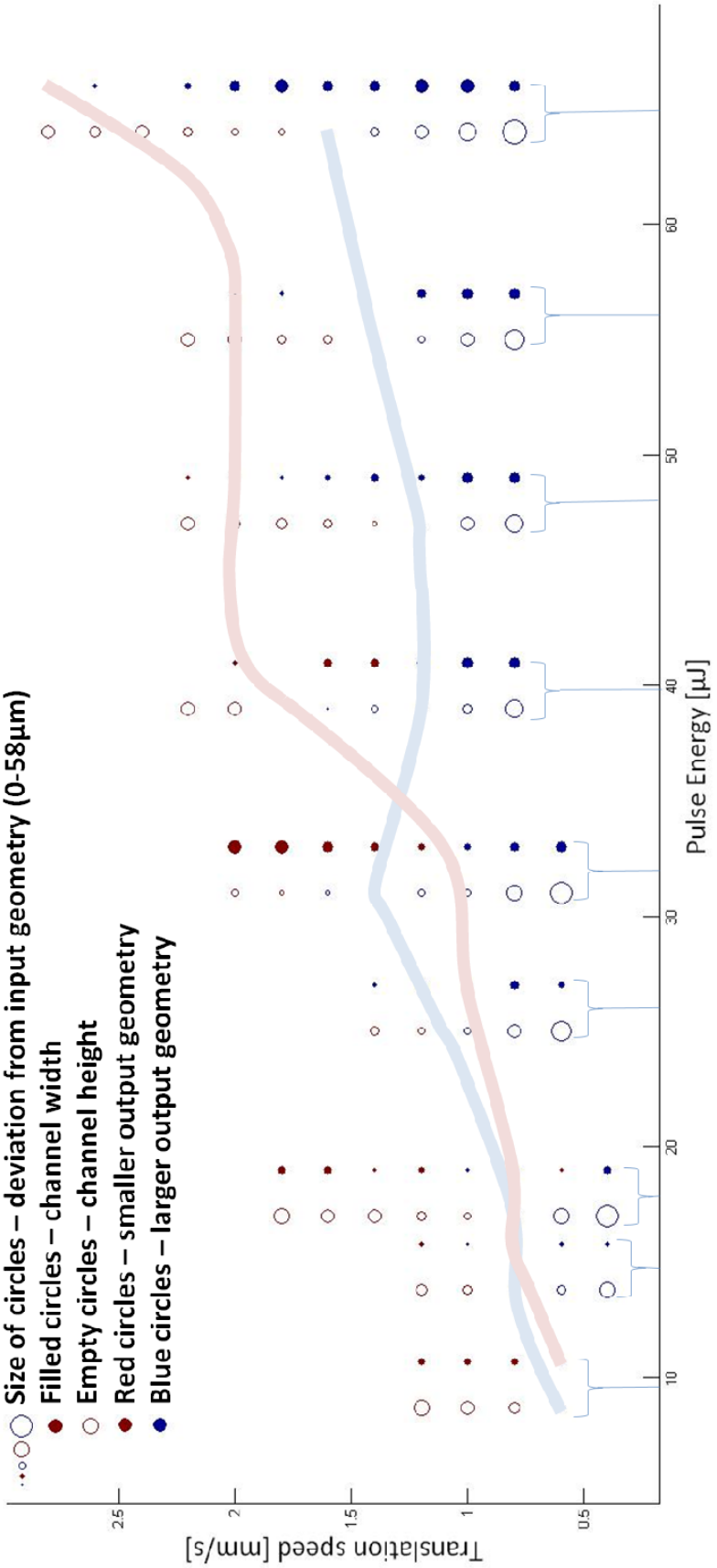

Figure 24 *Scatter plot of deviation from design geometry of cross section of bottom side ablated channels. Red and blue traces indicates best agreement to design geometry for width and height respectively*

Edge roughness

In Figure 25 a typical track edge for bottom side written tracks is shown. Dimensions of the roughness at the edges of an ablated region are found to be below 1 µm. There is also a formation of rims on the surface of the sample next to an area of ablated material. This is probably explained by a thin layer of melted material under the ablated region that is pushed out from the focal volume by plasma driven pressure [26, 27]. Other forces that would drive the melt towards the center of the laser focus, primarily thermocapillary flow are small compared to the plasma pressure. [27]

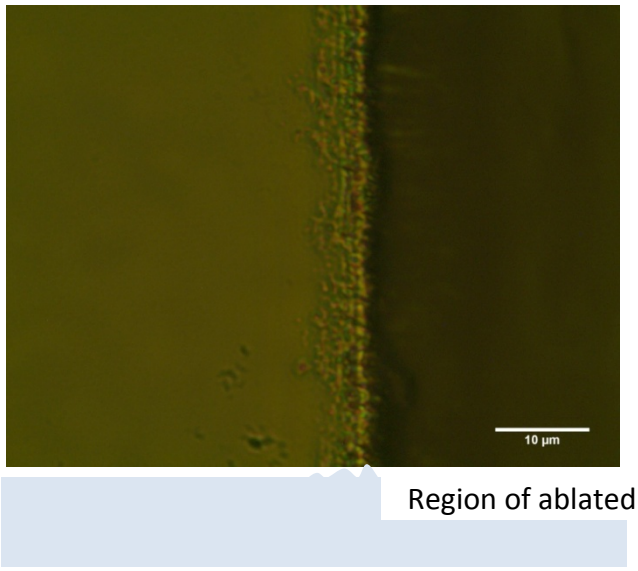

Figure 25 *Picture of a typical edge at 100X magnification. The rims in the illustration are exaggerated, from literature a typical height of these can be taken as 100 nm.*

5.4 Discussion

Ablation thresholds

There are no values to refer to in literature which are for the same parameters as used here and for thru material focusing. The threshold energies are working parameters for these experimental details and material. Fluence thresholds require a more precise determination of the $1/e^2$ radius. According to Eq. 4.6 the slope of the fitted function for obtaining threshold gives an experimental value of the $1/e^2$ radius at the interaction plane. As seen in Figure 19, the slopes are different for different number of pulses which likely is explained by the fact that this is only valid when obtaining single shot thresholds.

One weakness of this experiment is that the focusing is too strong. If a weaker focusing lens or objective would be used, the energy is distributed over a larger area since the beamwaist gets larger. In the case of stronger focusing it is very difficult to get good data since the difference in diameter between low energy/fewer pulses compared to higher energy/more pulses is smaller than it would be for weaker focusing. For this reason, measurements of crater diameter were meaningless for less than 30 overlapping pulses. Another weakness is that under ps-pulses in contrast to fs-pulses the edges of the ablated crater suffers from cracks, resulting in difficulties measuring the crater's diameter with good accuracy.

Top- vs bottom side ablation

The shape of the cross section was designed to be rectangular. However, all topside tracks yield the same V-shape as seen in Figure 21. This is probably explained by distortion and shadowing of the beam. When the focus is moved deeper into the material, half the beam propagates in air and the other half in the material. Due to this distortion and/or shadowing the photon density decreases and critical intensity is not reached. When the beam is translated laterally it again propagates in air and is not disturbed. Since the shadowing of the beam occurs when material obstrucs half of the converging beam it seems reasonable that the V-shaped profile should correspond to the angle of the converging beam. The numerical aperture of the objective is 0.45, n=1 is the index of refraction in the immersing medium, θ_{max} is calculated according to $n\ sin\theta_{max} = NA$. This gives a value of θ_{max} = 26.7° which is in good agreement to measurements of the cross section which gives a half cone angle of 27°.

When writing on the bottom side, it was found that the shape of the cross section is depending on the combination of translation speed and pulse energy. This is ascribed to the integrated incubation in the region with energy below ablation threshold. When the cross section is deep and curved, the range of the incubation- and thermal effects probably exceeds the range of ablation of subsequent moves made into the sample. In this scenario, incubation effects would accumulate and contribute to a deeper and more curved cross section. As pulse energy increases the gradient becomes weaker and for slower translation the integrated incubation reaches further out from the core of the focus. Consider figure 26 where it is shown that for pulse energy well above threshold the area of incubation grows to a large bulb compared to that of lower pulse energy. In an attempt to analyze the geometry of the cross sections to obtain fluence thresholds, ablation rate, incubation range etc. it was seen that the data shows expected behavior. However, the fact that the cross section is done with several steps into the sample and perpendicular to the translation direction, the situation becomes somewhat complex. Refinements to make an experimental design that is more likely to relate to a reliable model is proposed in the outlook.

In the case when the bottom of the track is flat, the incubated part of the material from the preceding scan is ablated in the next and no accumulation of incubation occurs.

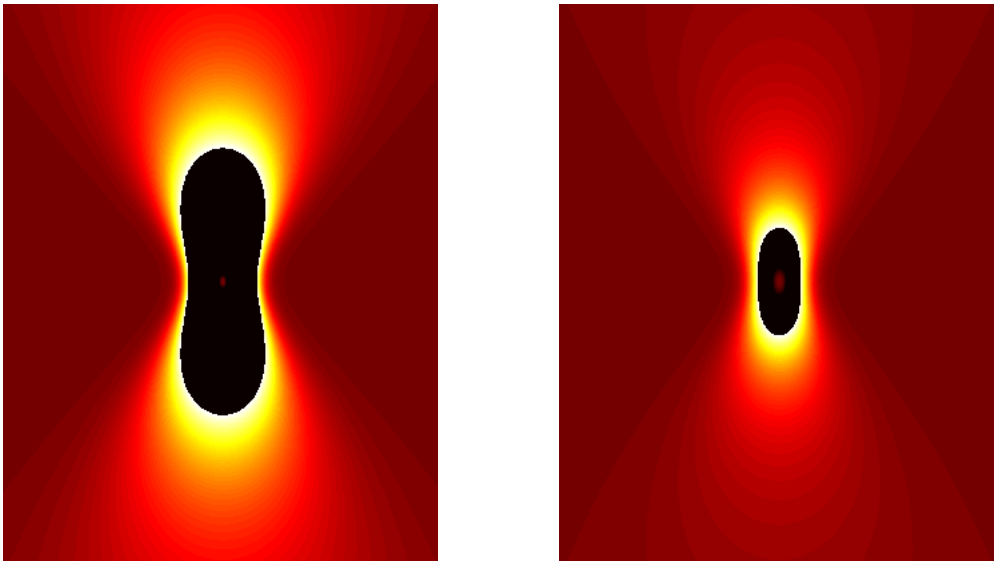

Figure 26 *Comparison of energy density between lower and higher pulse energies, sagital plane of a focused beam in vacuum. These illustrations must be considered with caution since they are not true for how the energy is distributed when the beam is focused into, and especially thru the material. However, they give a picture of how the energy is distributed and how the gradient behaves.The intensity distribution is based on a beamwaist of 4 µm and the truncated region is some arbitrary intensity.*

5.5 Conclusions and outlook

A system for direct picosecond laser writing with the capability of position synchronized laser firing, online monitoring and direct microscopic evaluation was assembled and tested. Surface structuring by ablation with potential application in microfluidics was done. A thorough investigation of parameter impact on the output geometry was done. Control over those process parameters makes more complex geometries possible. Advantages and complications with bottom side ablation, compared to top side ablation, were found. The input design is more flexible but pulse energy and translation speed has to be chosen carefully since the result is more affected by incubation effects. Focusing complications has not been found to be a problem in the picosecond regime. The roughness of edges and surfaces are within the limits for many applications. Even smoother structures can be achieved by a rapid post processing by a wet etch or heat treatment e.g. in a furnace or by CO_2 laser irradiance.

Ablation threshold energies were found for top side focusing and 10 overlapping pulses. For bottom side focusing, threshold energies for 30 to 60 pulses were obtained. These are working parameters for experimental details and sample thickness. Effects that affect the ablation threshold, believed to be thermal, were observed. It confirmed by in-situ observations that the damage threshold increase when the laser repetition rate was decreased.

Programs for controlling the translation systems motion for complex geometries and for direct image import was made. These increase design flexibility and makes operation of the system fast and easy. The position synchronized laser firing was tested for image import down to a resolution of 0.60 μm for a resolvable output of voxels (3D pixels) consisting of densified material in the bulk.

With an integrated and performing setup for direct laser writing there is a good basis for designing and making complex structures for microfluidic networks and to develop the system further for writing waveguide and grating structures in bulk material and in optical fibers. The system shows capabilities for making complex structured microfluidic chip with the possibility to tailor the design in three dimensions. The intention would be to make improvements from a microfluidic point of view. There are also a large variety of physio-chemical approaches that would enhance precision and light-matter interactions.

Improvement in the threshold investigations could easily be done by using a weaker focusing, e.g. a 4X microscope objective. Also thermal effects could be investigated by letting multi pulse thresholds depend on laser repetition rate. Probably the change in threshold would decrease down to some cut off repetition rate where thermal effects no longer affect ablation thresholds. If thermal effects can be shown, these could be separated from permanent incubation effects due to material alterations. By scanning the bottom side of the sample, ablation straight tracks as described but with no collateral moves and using a low NA objective, incubation range and energy thresholds could be investigated in a novel manner.

The motivation to investigating thermal effects and incubation range is that it would gain further control over material interaction and increase resolution. This is very important in refractive index tailoring, including index modulation, which is on a smaller scale that that of channel ablation. To further conclude, this work and proposed investigations is a solid base with understanding of light-material interaction, control over system performance, programming and operation. The employment of other wavelengths as complement, competition or used superimposed must not be forgotten.

6 References

[1] D. Hülsenberg, A. Harnisch, and A. Bismarck, Microstructuring of Glasses, Springer, 2009.

[2] R. Martinez Vazquez, R. Osellame, M. Cretich, M. Chiari, C. Dongre, H. Hoekstra, M. Pollnau, H. van den Vlekkert, R. Ramponi, and G. Cerullo, Analytical and Bioanalytical Chemistry 393 (2009) 1209.

[3] S. Kawata and T. Sugiura, Opt. Lett. 17 (1992) 772.

[4] H. Hunt and J. Wilkinson, Microfluidics and Nanofluidics 4 (2008) 53.

[5] M. L. Chabinyc, D. T. Chiu, J. C. McDonald, A. D. Stroock, J. F. Christian, A. M. Karger, and G. M. Whitesides, Analytical Chemistry 73 (2001) 4491.

[6] G. L. Mitchell, J Quantum Electron 13 (1977) 173.

[7] A. Manz, N. Graber, and H. M. Widmer, Sensors and Actuators B: Chemical 1 (1990) 244.

[8] K. Ramser, J. Enger, M. Goksör, D. Hanstorp, K. Logg, and M. Käll, The Royal Society of Chemistry 5 (2005) 431.

[9] R. C. Jaeger, Lithography. Introduction to microelectronic fabrication, Prentice Hall, 2002.

[10] G. D. Valle and et al., Journal of Optics A: Pure and Applied Optics 11 (2009) 013001.

[11] R. Kashyap, Fiber Bragg Gratings, Academic Press, 1999.

[12] E. Hecht, Optics, Pearson Education, 2001.

[13] H. Zhang, S. M. Eaton, J. Li, and P. R. Herman, Opt. Lett. 31 (2006) 3495.

[14] A. K. Varshneya, Fundamentals of Inorganic Glasses, Academic Press, 1994.

[15] Y. Pan, F. Inam, M. Zhang, and D. A. Drabold, Physical Review Letters 100 (2008) 206403.

[16] F. Moser and F. Urbach, Physical Review 102 (1956) 1519.

[17] B. C. Stuart, M. D. Feit, S. Herman, A. M. Rubenchik, B. W. Shore, and M. D. Perry, J. Opt. Soc. Am. B 13 (1996) 459.

[18] R. M. Wood, 1986, A. Hilger (Bristol and Boston) Laser Damage in Optical Materials.

[19] M J Soileau , W. E. Williams, E. W. V. Stryland, T. F. Boggess, and A. L. Smirl, Natl Bur. Stand. (US) Spec. Publ. 669 (1984) 387.

[20] C. B. Schaffer, A. Brodeur, and E. Mazur, Meas. Sci. Technol. 12 (2001)

[21] L. V. Keldysh, Soviet Physics JETP 20 (1965) 1307.

[22] P. P. Rajeev, M. Gertsvolf, P. B. Corkum, and D. M. Rayner, Physical Review Letters 102 (2009) 083001.

[23] C. B. Schaffer, J. F. García, and E. Mazur, Applied Physics A: Materials Science & Processing 76 (2003) 351.

[24] J. M. Liu, Opt. Lett. 7 (1982) 196.

[25] B.-Y. Adela and et al., Journal of Physics D: Applied Physics 40 (2007) 1447.

[26] K. J. Ghaleh, N. Mansour, D. Ashkenasi, and H.-J. Hoffmann, Optics Communications 246 (2005) 213.

[27] A. Ben-Yakar and R. L. Byer, Journal of Applied Physics 96 (2004) 5316.

7 Appendix

7.1 Alignment procedure

In order to align the system the following scheme was worked out.

1. Make a course alignment of the whole system using the HeNe reference beam.

2. Align the sample with the XY-translation plane

   Place a glass sample in the holder and a mirror on the table under the sample. Use the interference between the reflection from the glass sample and the mirror to align the sample holder with the XY translation plane. When the fringes are as stable as possible under translation of the sample it is aligned with the XY-translation plane. In a major part of the translation the sample should be within a deviation of maximum 150nm. A larger deviation at a specific position is related non-optimal flatness in the translation stage.

3. Align the HeNe reference beam

   Use a mirror made from a glass sample (by depositing aluminum in a vaporization chamber) placed in the sample holder and align the HeNe beam so that it is completely collinear with itself. Use BS1 and M1, the aperture can be useful. Also use the outgoing reflection from the HeNe outcoupling mirror.

4. Align the IR beam

   The IR beam will be aligned when it hits BS2 at the same spot as the HeNe beam goes thru and at an incident angle that makes the two beams coaxial all thru the system. Use two mirrors outside the system, delivering the IR beam, separated minimum 50cm. Fine tune using the Dichroic mirror 1 and onr of the external mirrors guiding the IR beam into the system

5. Adjusting the microscope objective

   After a coarse adjustment fine tune the microscope objective by observing the reflections from the lens surfaces and overlap those as good as possible.

It was found that the sample could be aligned within 150nm of the translation plane with the exception from two ranges were the deviation increased up to approximately 0.6 µm. This position and deviation is consistent with the data on flatness supplied by the manufacturer.

After this procedure the beam delivery is aligned to a sample collinear with the translation plane. If the sample holder or microscope objective is misaligned, those are to be adjusted, not beam delivery. Start by aligning the sample holder using the interferometer. After a coarse alignment, fine tune until maximum stability in the interference fringes are determined.

7.2 Laser Control schematic

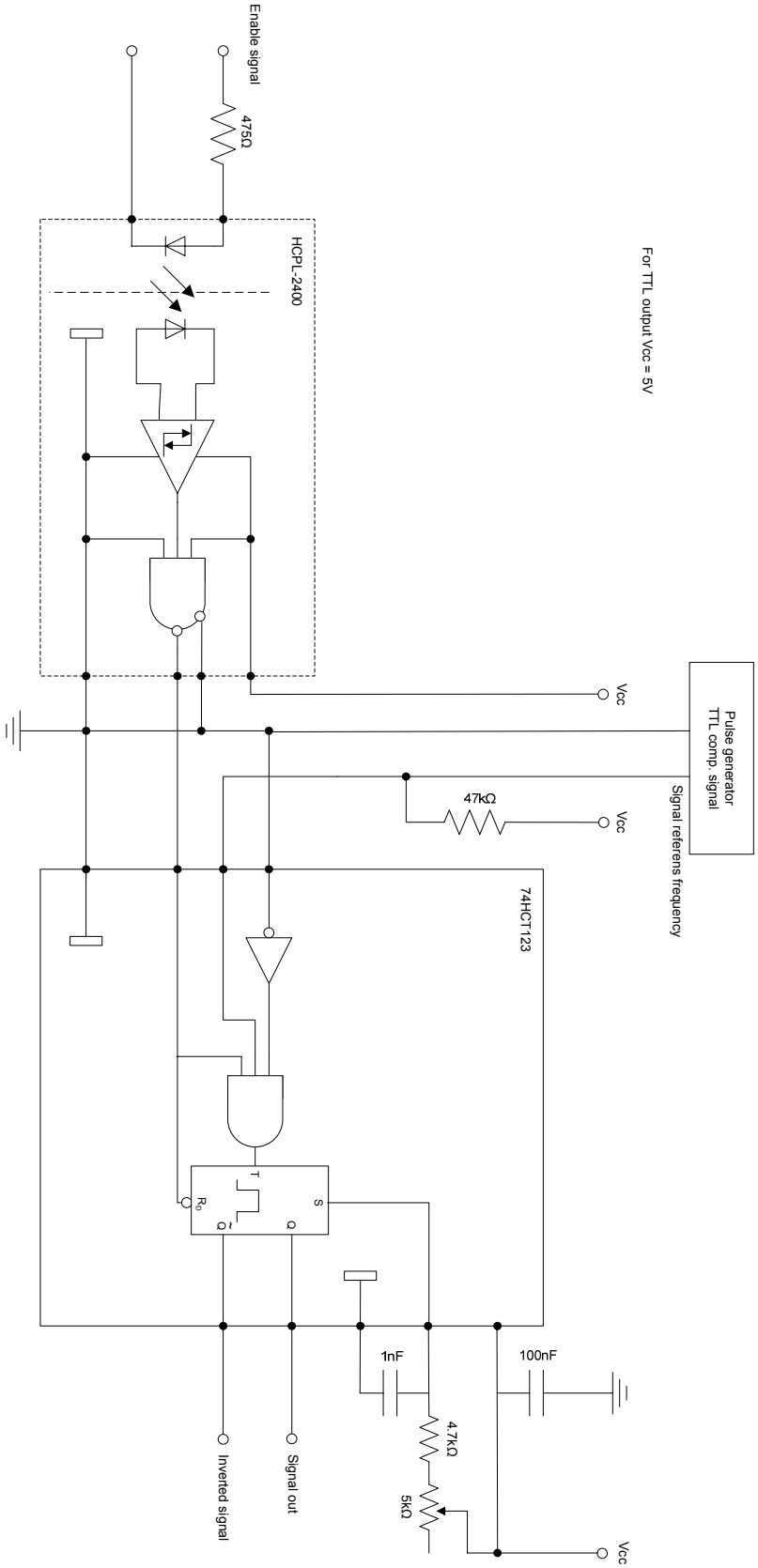

7.3 Corning® EAGLE2000™ Specifications

Glass Type – Alkaline Earth Boro-Aluminosilicate
Forms Available – Fusion drawn sheet
Principal Uses – Substrates for Active Matrix flat panel displays

Properties

Where applicable, units are stated in Metric and English

Mechanical

	Metric	English
Density (20°C, 68°F)	2.37 g/cm^3	147.9 lb/ft^3
Young's Modulus	70.9 GPa	10.3 Mpsi
Poisson's Ratio	0.23	0.23
Shear Modulus	28.9 GPa	4.2 Mpsi

Vickers Hardness 642
(200 gm load, 25 sec dwell)

Thermal Expansion

0 - 300°C	31.8 x 10^{-7}/°C (0 - 300°C)	17.7 x 10^{-7}/°F (32 - 572°F)
Room Temperature To Setting Point	36.1 x 10^{-7}/°C (25 - 670°C)	20.1 x 10^{-7}/°F (77 - 1238°F)

Electrical

Log_{10}Volume Resistivity (ohm-cm)

12.5	(250°C, 482°F)
10.5	(350°C, 662°F)
8.5	(500°C, 932°F)

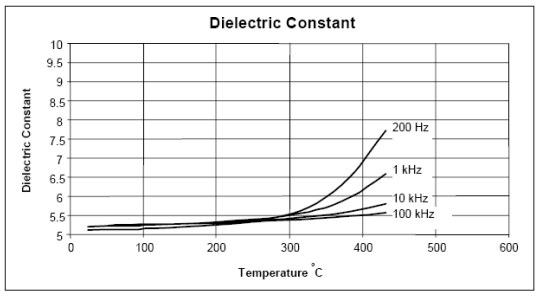

Dielectric Constant: 5.181
(20°C/68°F – 1 kHz)

Thermal Conductivity

Thermal Conductivity is a calculated value, and is equal to the product of the Thermal diffusivity multiplied by Specific Heat multiplied by Density of the glass.

Temp (°C)	Specific Heat (cal/gm-°K)	Thermal Diffusivity (cm^2/sec)	Thermal Conductivity (cal-cm/cm^2-sec-°K)
23	0.176	0.00511	0.00213
50	0.185	0.00512	0.00225
100	0.201	0.00510	0.00244
200	0.226	0.00507	0.00272
300	0.244	0.00503	0.00291
400	0.260	0.00499	0.00307
600	0.288	0.00507	0.00344

Viscosity

Working Point (10^4 poises)	1321°C	2410°F
Softening Point ($10^{7.6}$ poises)	985°C	1805°F
Annealing Point (10^{13} poises)	722°C	1332°F
Strain Point ($10^{14.5}$ poises)	666°C	1231°F

Chemical

Weathering: 1
Weathering is defined as corrosion by atmospheric-borne gases and vapor such as water and carbon dioxide. Glasses rated 1 will almost never show weathering effects, those rated 2 will occasionally be troublesome, particularly if weathering products cannot be removed, those rated 3 require more careful consideration.

Durability:
Durability is measured via weight loss per surface area after immersion. Values are highly dependent upon actual testing conditions. Data is reported for EAGLE^{2000} and Corning 1737 glasses run concurrently. Unless otherwise noted, concentrations refer to weight percent.

Dielectric Constant: 5.181
(20°C/68°F – 1 kHz)

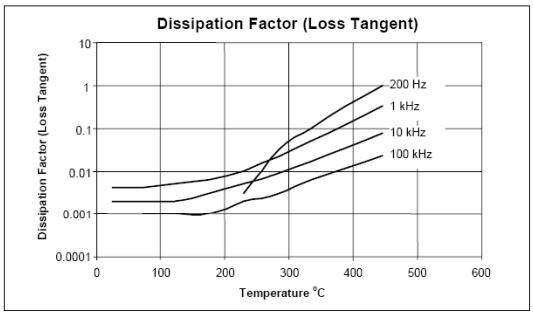

Loss Tangent: 0.40%
(20°C/68°F – 1 kHz)

Reagent	Time	Temp	Weight Loss (mg/cm^2) EAGLE^{2000}	Corning 1737
HCl – 5%	24 hrs	95°C	0.30	0.46
HNO_3 – 1M	24 hrs	95°C	0.17	0.24
HF – 10%	20 min	22°C	3.71	6.34
NH_4F:HF – 10%	20 min	22°C	0.75	1.17
1HF:10HNO_3	3 min	25°C	1.35	2.01
1HF:100HNO_3	3 min	25°C	0.40	0.46
DI H_2O	24 hrs	95°C	0.00	0.01
Na_2CO_3 – 0.02N	6 hrs	95°C	0.14	0.17
NaOH – 5%	6 hrs	95°C	1.61	1.76

Total alkali content is approximately: 0.1 wt%
(Typical < 0.05 wt%)

Optical Wavelength	Refractive Index
435.8 nm	1.5170
480 nm	1.5131
486.1 nm	1.5126
546.1 nm	1.5090
589.3 nm	1.5068
643.8 nm	1.5050
656.3 nm	1.5046

Birefringence Constant
327 (nm/cm)/(kg/mm^2)

Transmittance

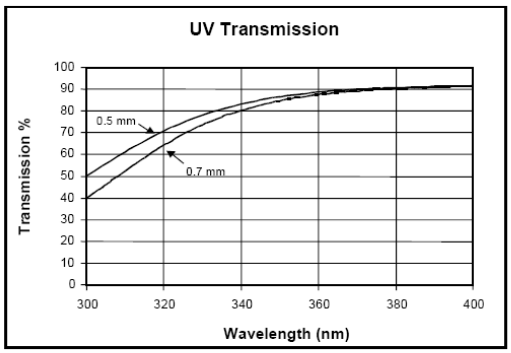

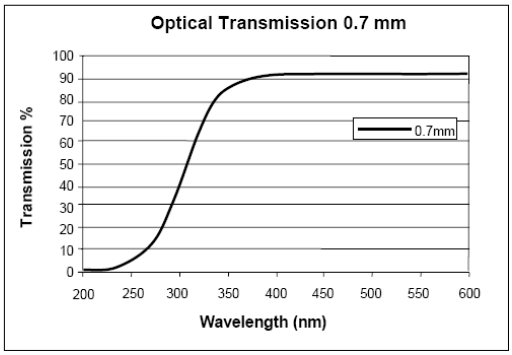

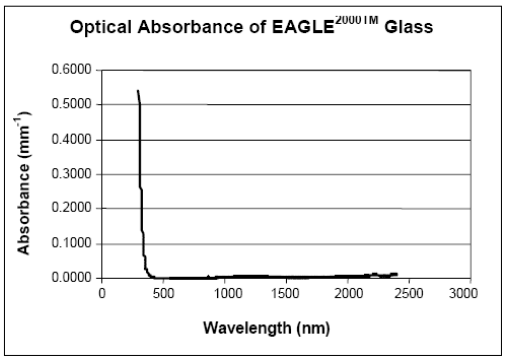

7.4 Aerotech motion stages specifications

Basic Model		ALS130-025	ALS130-050
Total Travel		25 mm (1 in)	50 mm (2 in)
Drive System		Linear Brushless Servomotor (BLMUC-95-A)	
Bus Voltage		Up to 80 VDC with a single 25-pin D connector; Up to 160 VDC with split feedback and power – two 25-pin D connectors	
Continuous Current	A_{pk}	2.94	
	A_{rms}	2.08	
Feedback		Noncontact Linear Encoder	
Resolution		0.0025 µm - 0.004 µm	
Maximum Travel Speed(1)		300 mm/s (12 in/s)	
Maximum Linear Acceleration		1g (10 m/s^2) (384 in/s^2) (No Load)	
Maximum Load(2)	Horizontal	12.0 kg (26.5 lb)	
	Side	10.0 kg (22.0 lb)	
Accuracy	HALAR(3)	±0.3 µm (±12 µin)	
	Standard	±2.0 µm (±80 µin)	±2.0 µm (±80 µin)
Repeatability		±100 nm	
Straightness and Flatness	Maximum Deviation	±1.0 µm (±40 µin)	±1.0 µm (±40 µin)
Pitch		5 arc sec	6 arc sec
Roll		5 arc sec	6 arc sec
Yaw		3 arc sec	3 arc sec
Nominal Stage Weight		3.0 kg (6.5 lb)	3.0 kg (6.5 lb)
Moving Mass		0.9 kg (2.0 lb)	1.1 kg (2.4 lb)
Construction		Aluminum Body/Black Anodize Finish	

Notes:

1. Maximum speed based on stage capability. Maximum application velocity may be limited by system data rate and system resolution.

2. Maximum load based on bearing capability. Maximum application load may be limited by acceleration requirements.

3. Available with Aerotech controllers.

4. Specifications are for single-axis systems, measured 50 mm above the tabletop.

Performance of multi-axis systems is payload and workpoint dependent. Consult factory for multi-axis or non-standard applications.

7.5 Cross section images

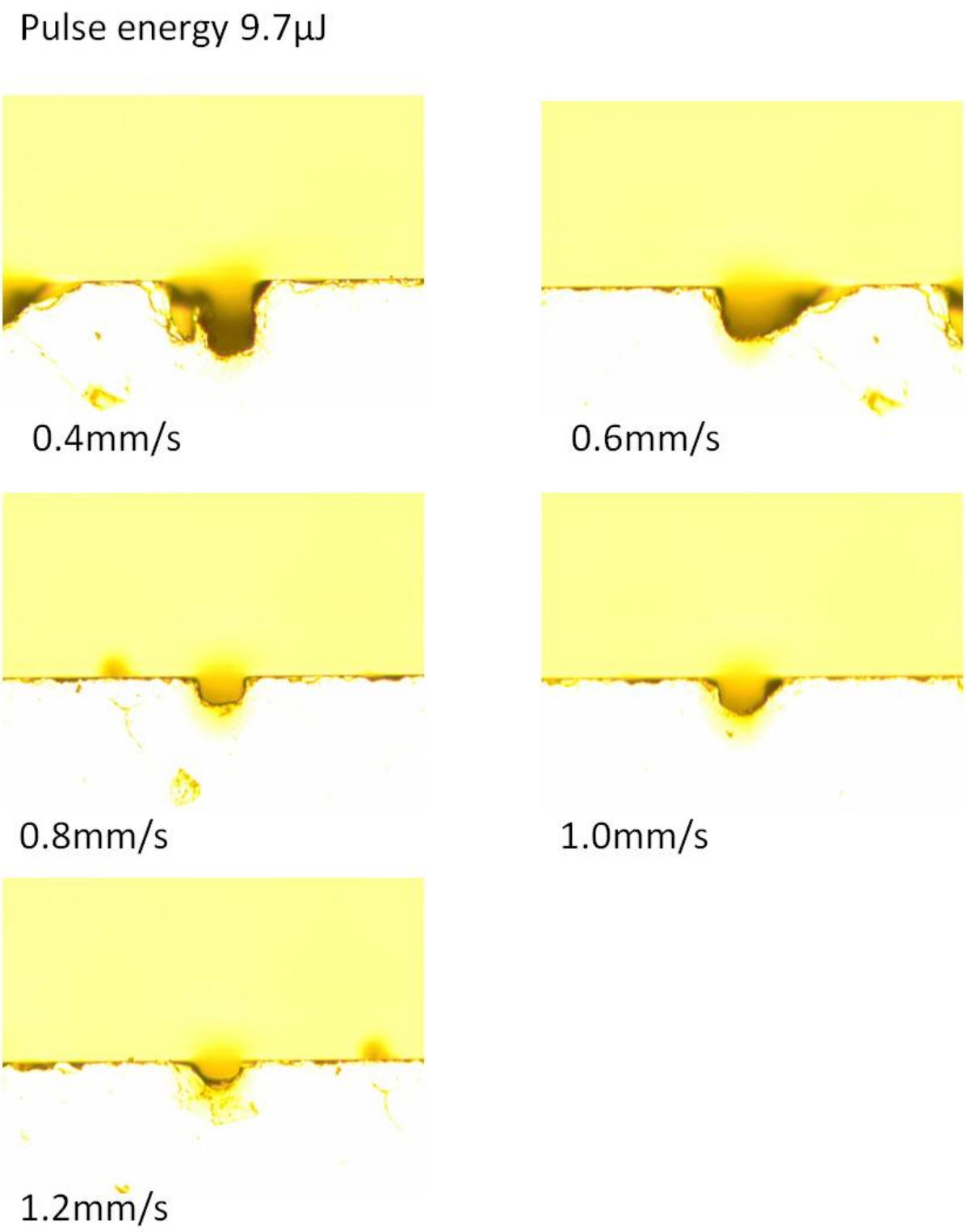

Pulse energy14.8μJ

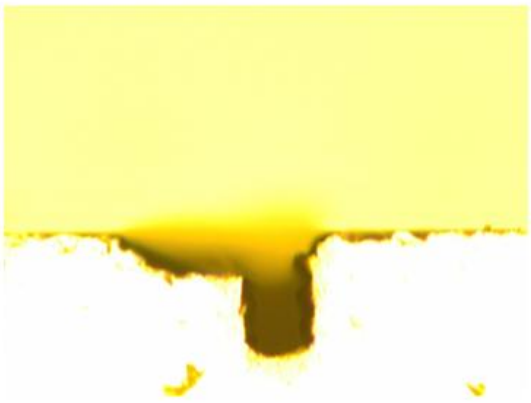

0.4mm/s

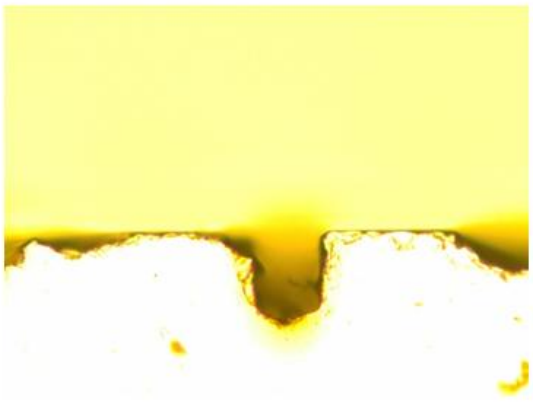

0.6mm/s

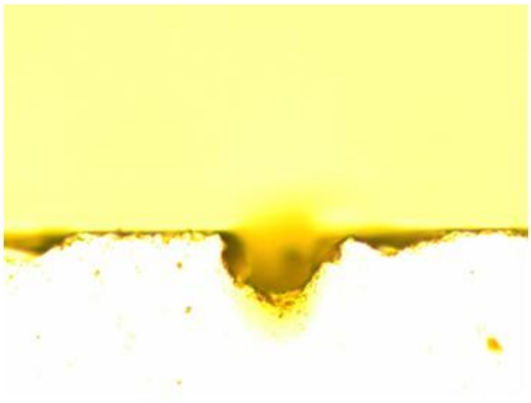

0.8mm/s

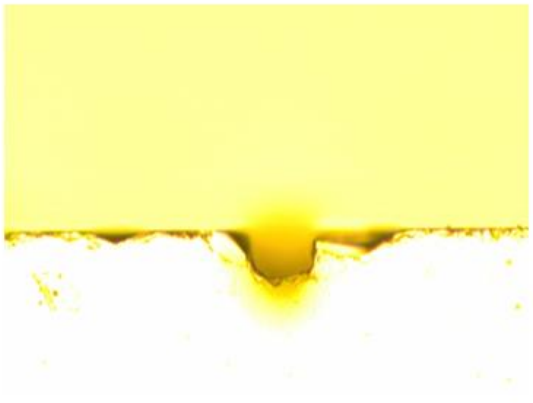

1.0mm/s

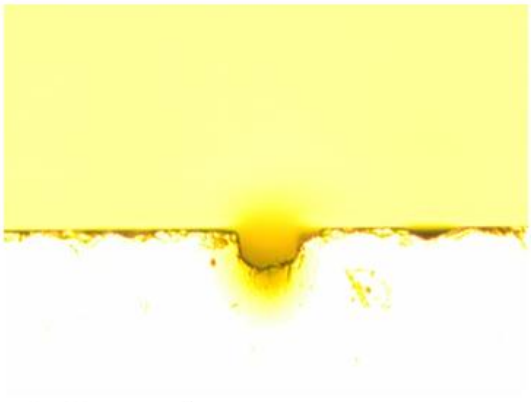

1.2mm/s

Pulse energy18μJ

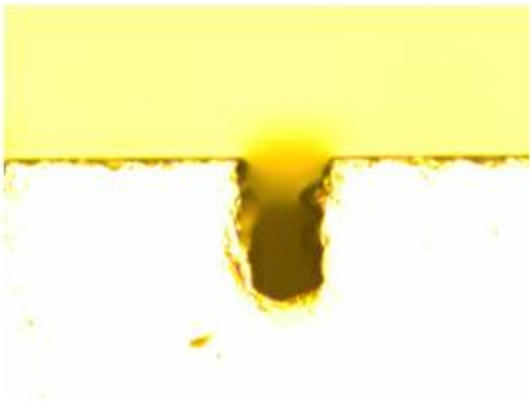

0.4mm/s

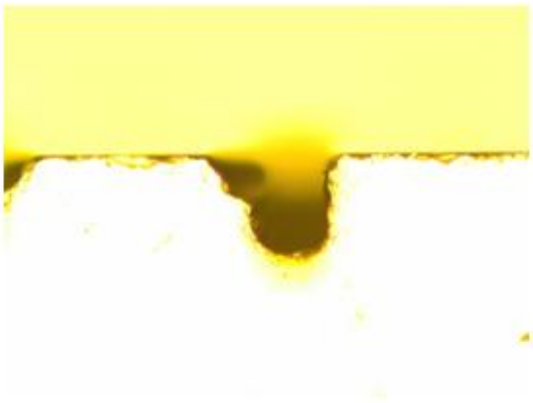

0.6mm/s

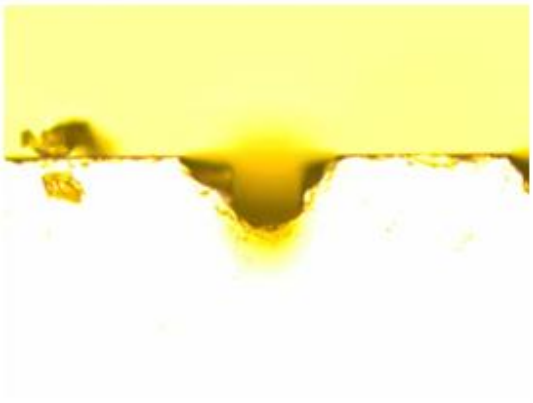

0.8mm/s

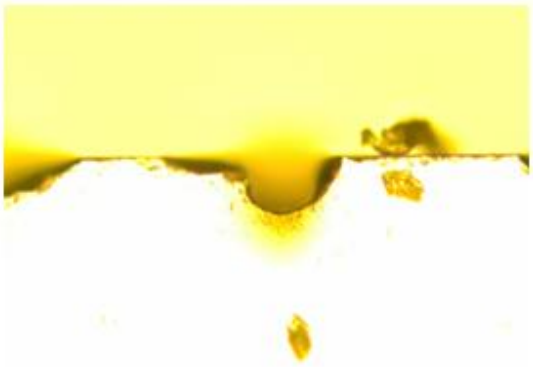

1.0mm/s

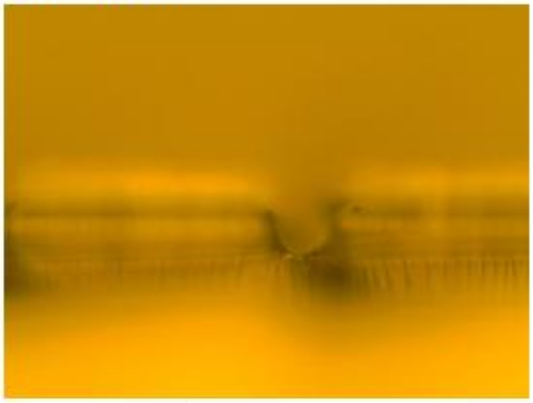

1.2mm/s

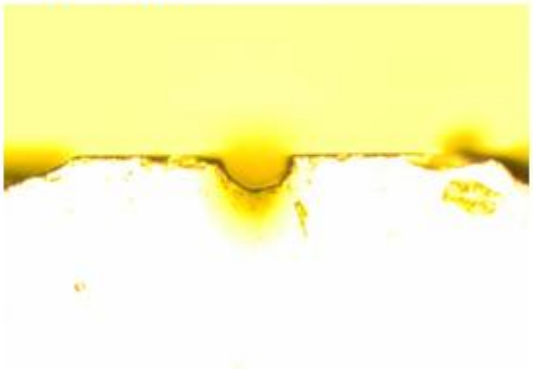

1.4mm/s

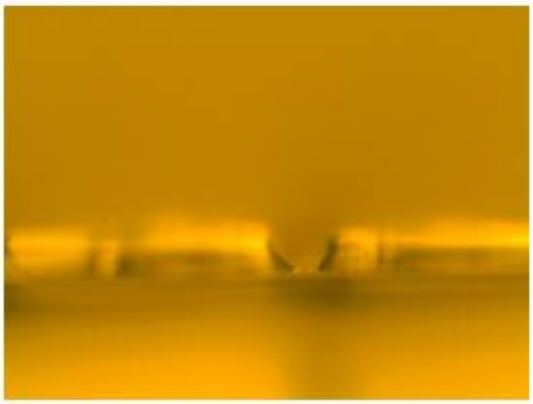

1.6mm/s

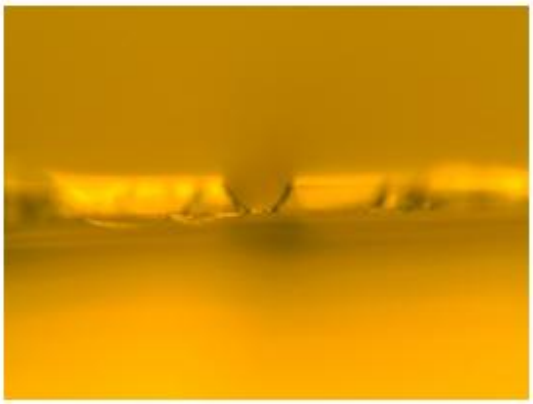

1.8mm/s

Pulse energy26μJ

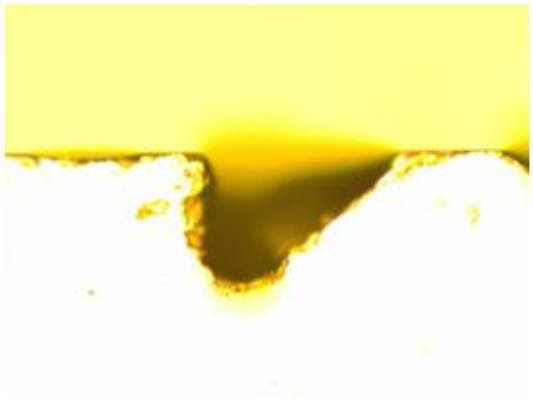

0.4mm/s

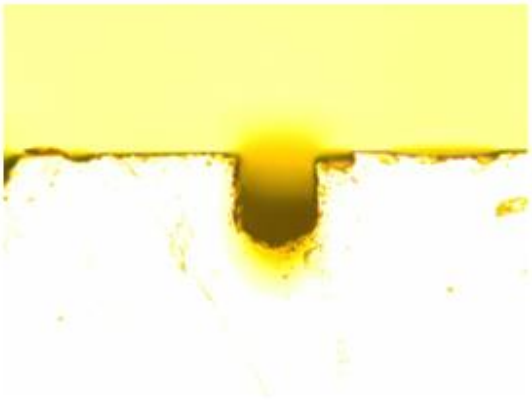

0.6mm/s

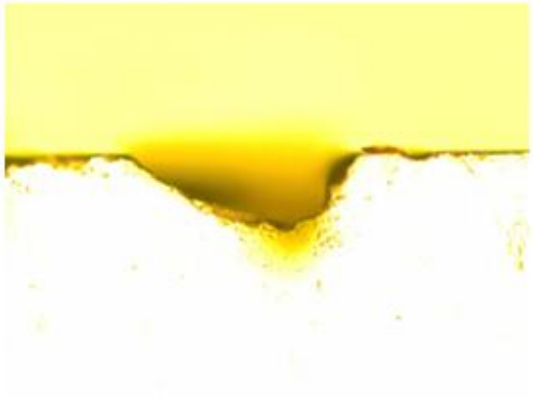

0.8mm/s

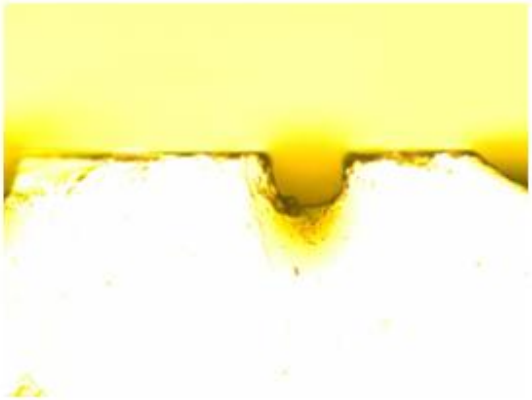

1.0mm/s

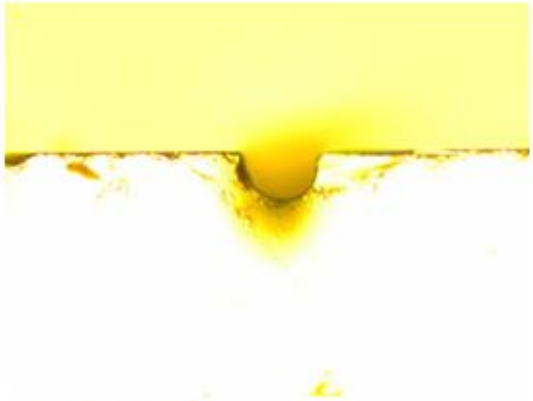

1.2mm/s

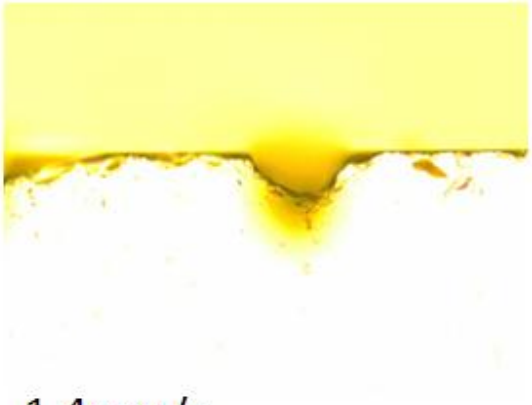

1.4mm/s

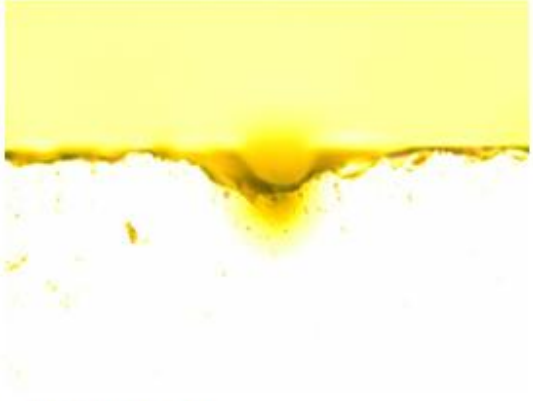

1.6mm/s

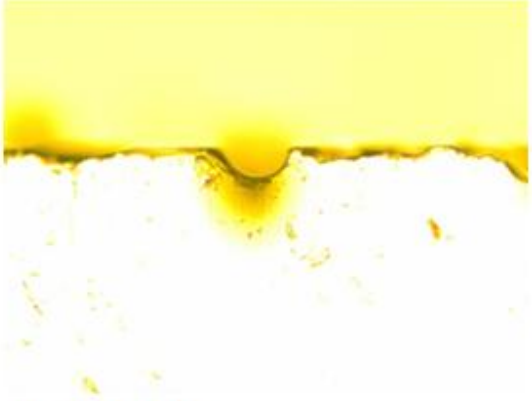

1.8mm/s

Pulse energy32μJ

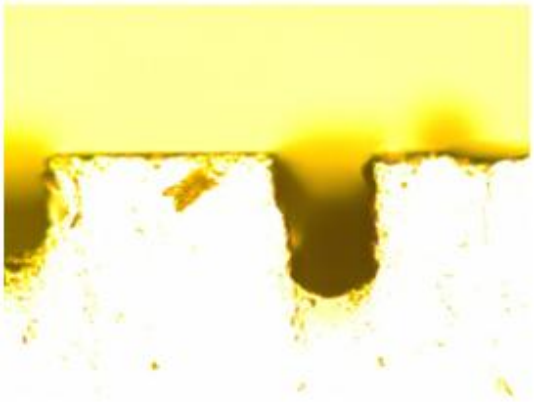

0.4mm/s

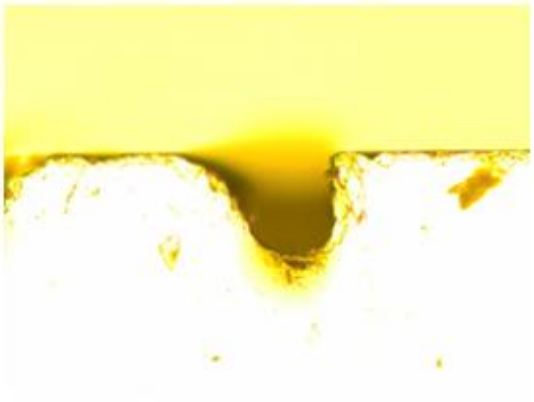

0.6mm/s

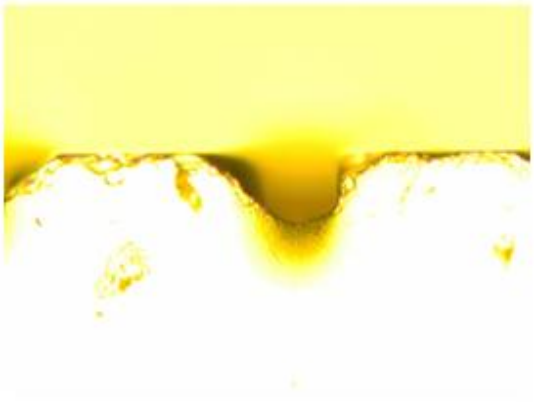

0.8mm/s

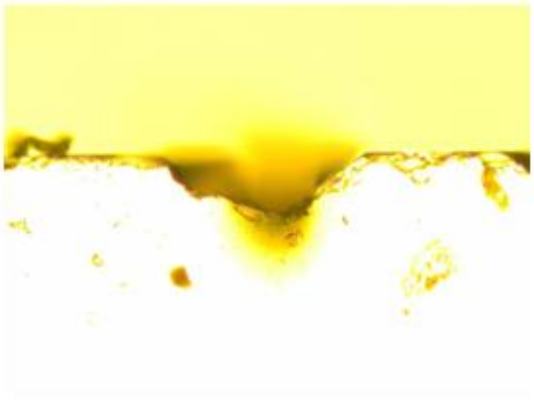

1.0mm/s

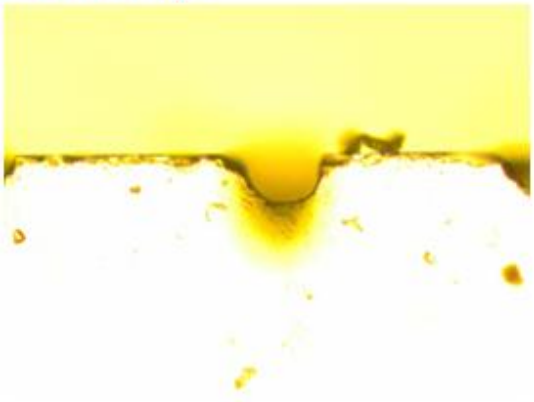

1.2mm/s

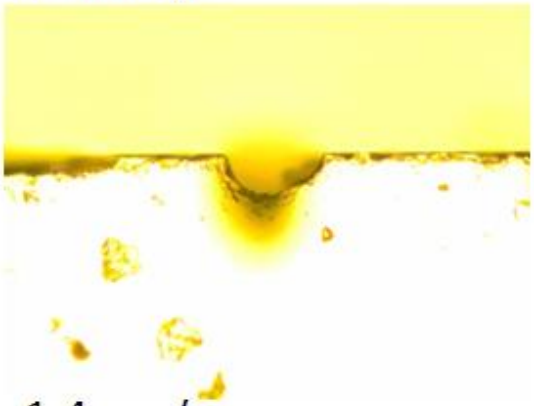

1.4mm/s

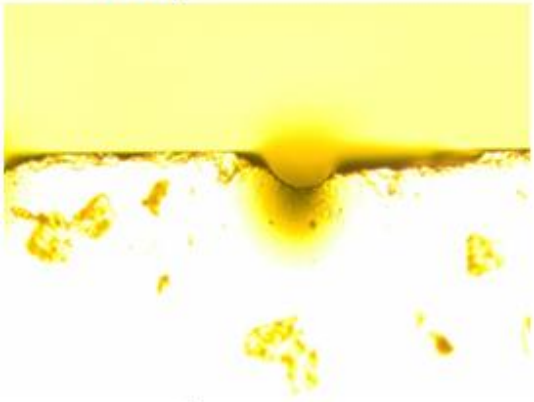

1.6mm/s

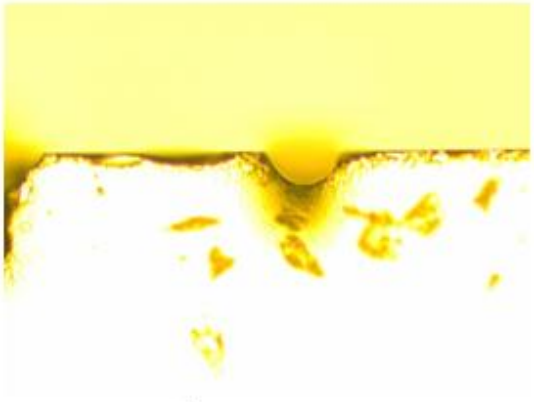

1.8mm/s

Pulse energy 40μJ

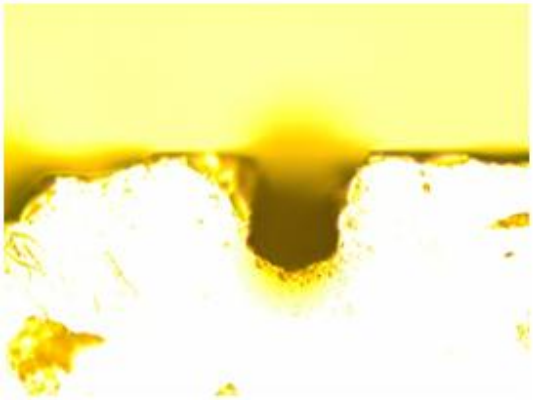

0.8mm/s

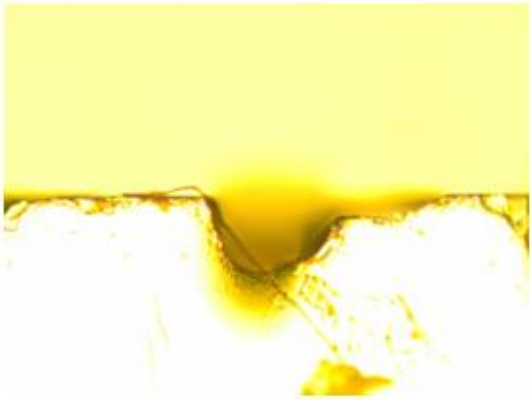

1.0mm/s

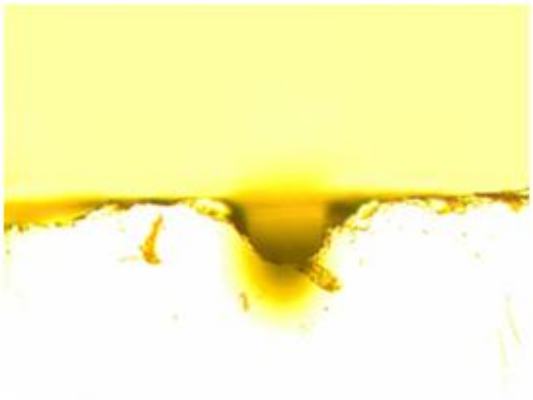

1.2mm/s

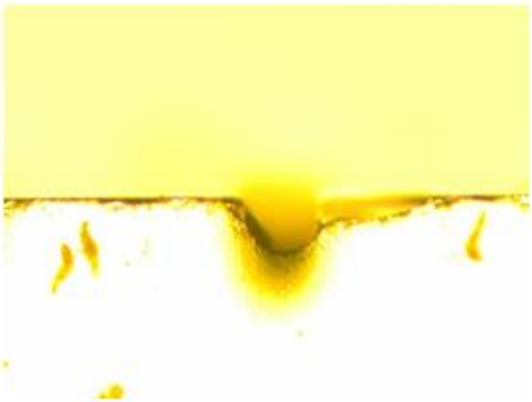

1.4mm/s

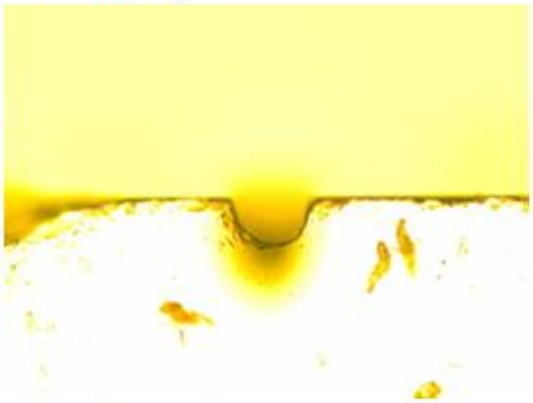

1.6mm/s

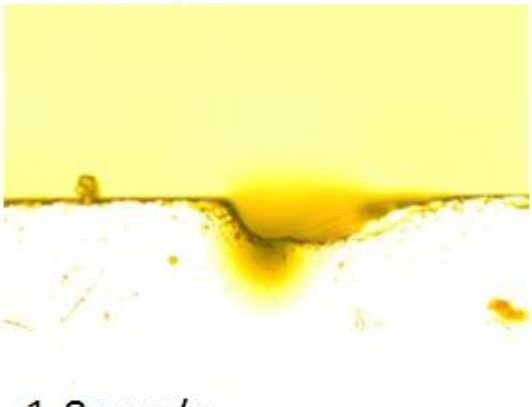

1.8mm/s

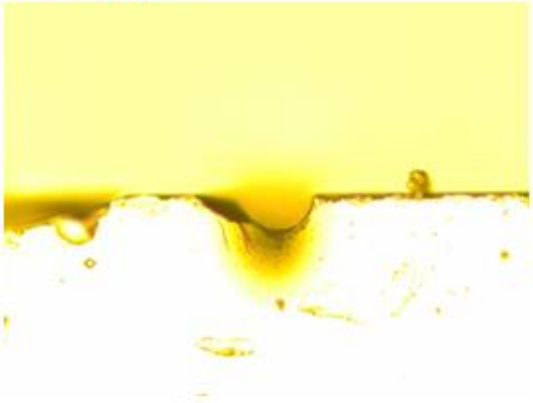

2.0mm/s

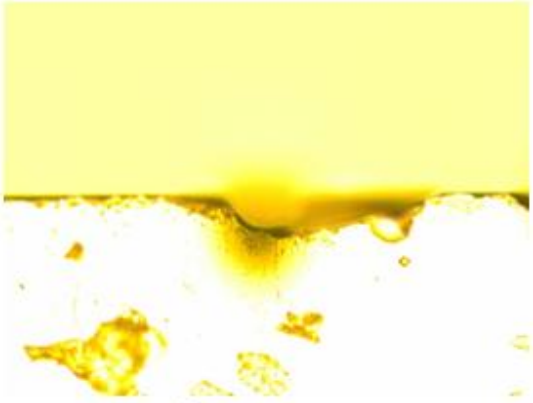

2.2mm/s

Pulse energy 48μJ

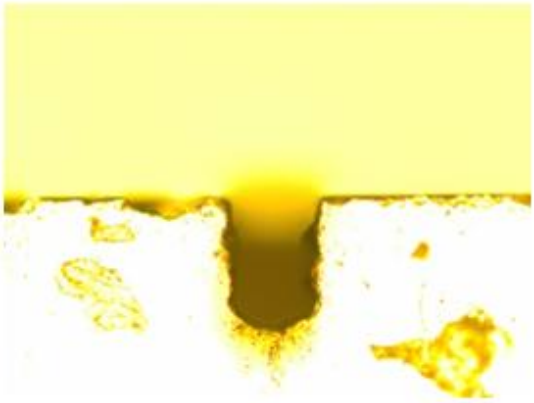

0.8mm/s

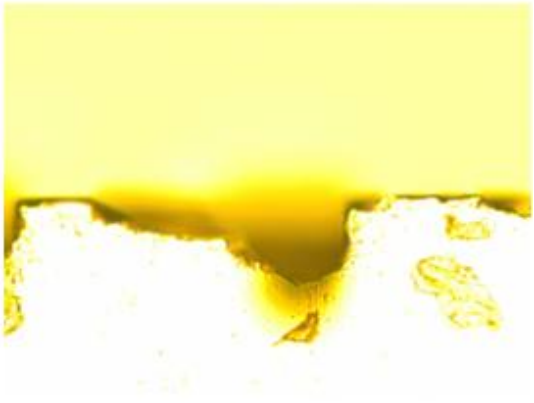

1.0mm/s

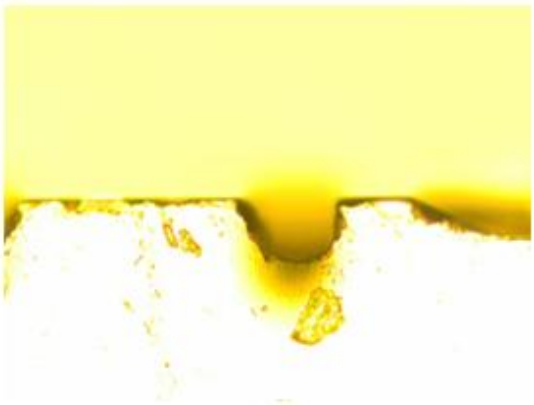

1.2mm/s

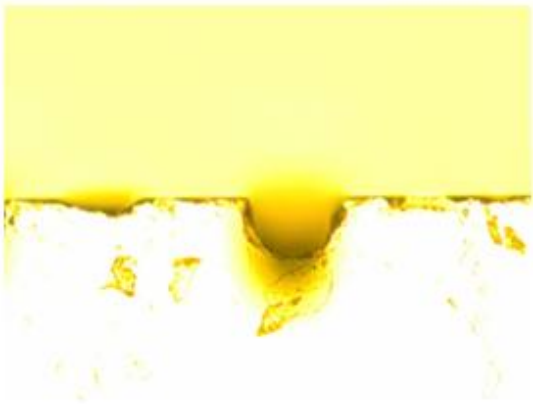

1.4mm/s

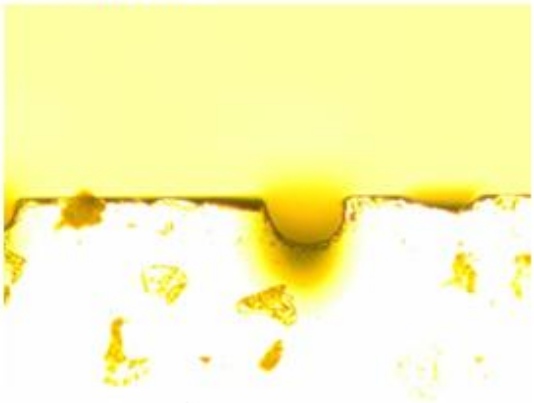

1.6mm/s

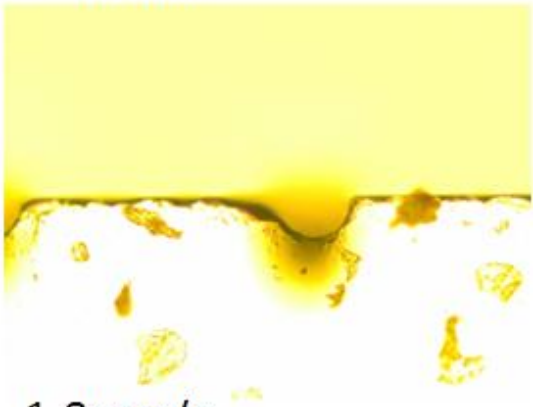

1.8mm/s

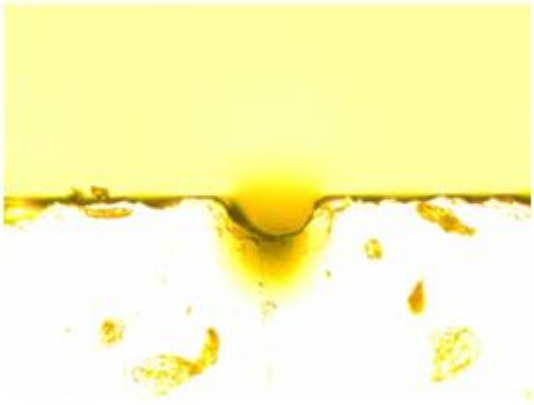

2.0mm/s

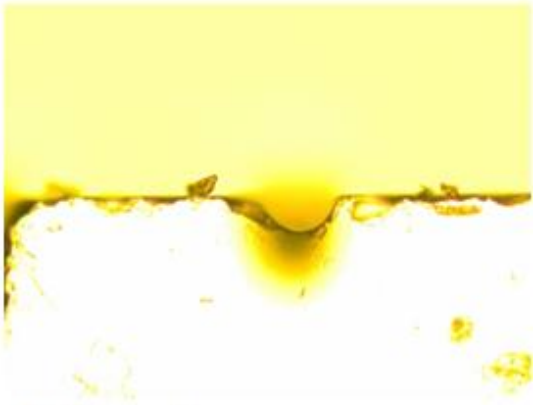

2.2mm/s

Pulse energy 56μJ

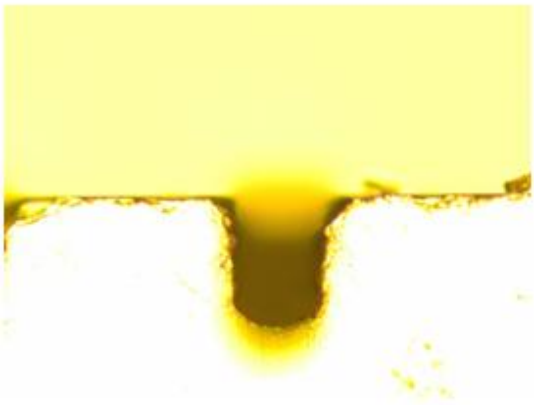

0.8mm/s

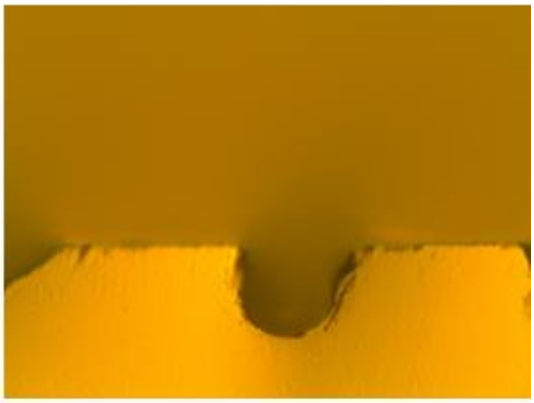

1.0mm/s

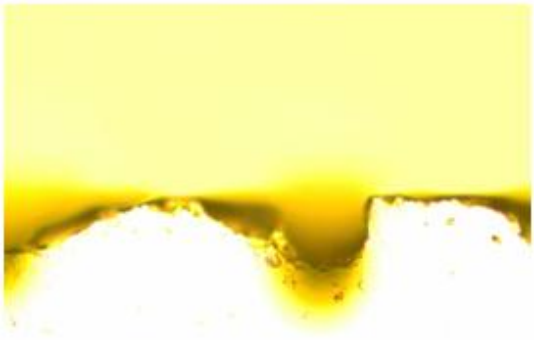

1.2mm/s

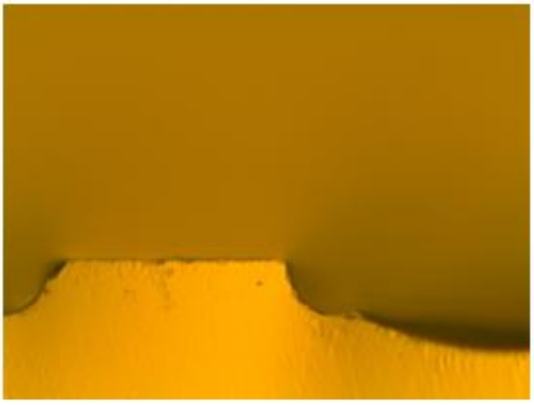

1.4mm/s

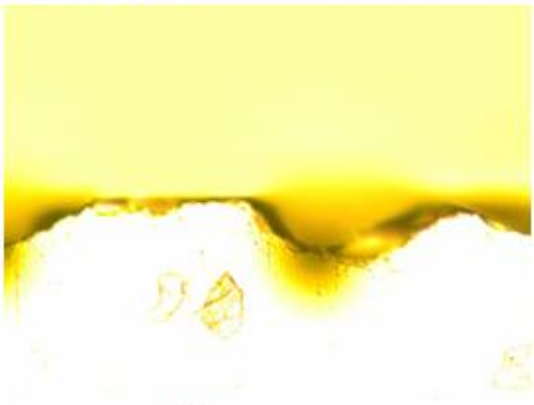

1.6mm/s

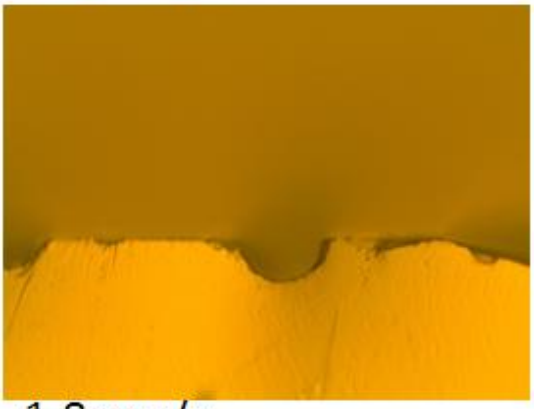

1.8mm/s

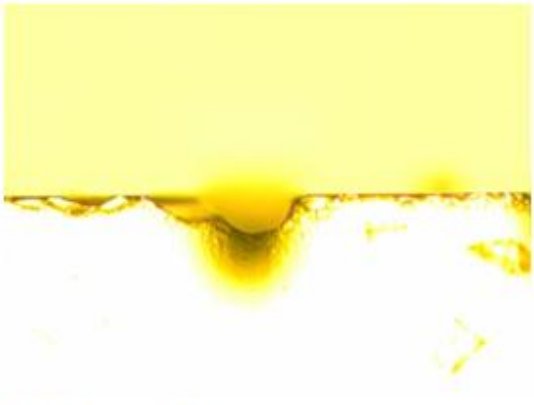

2.0mm/s

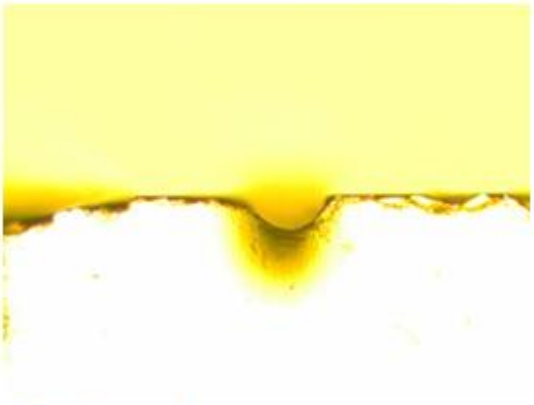

2.2mm/s

Pulse energy 65μJ

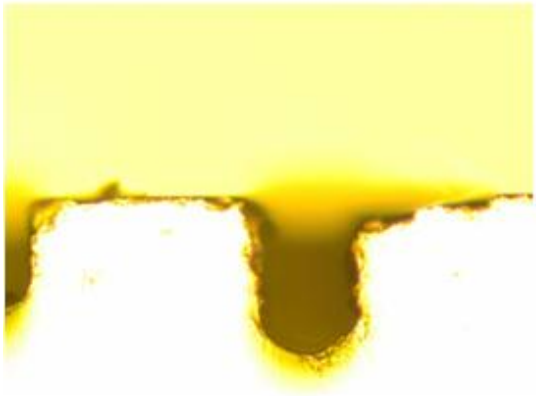

0.8mm/s

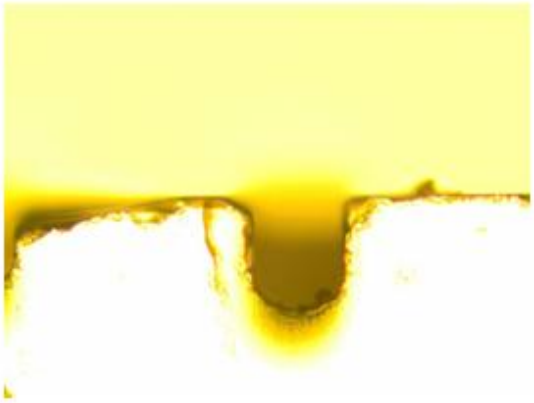

1.0mm/s

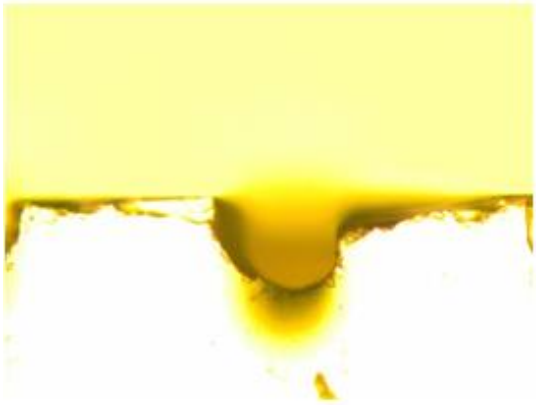

1.2mm/s

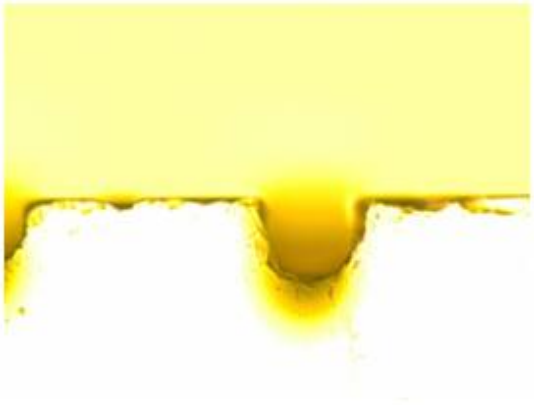

1.4mm/s

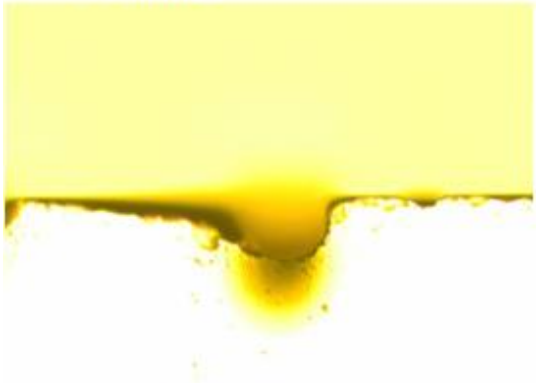

1.6mm/s

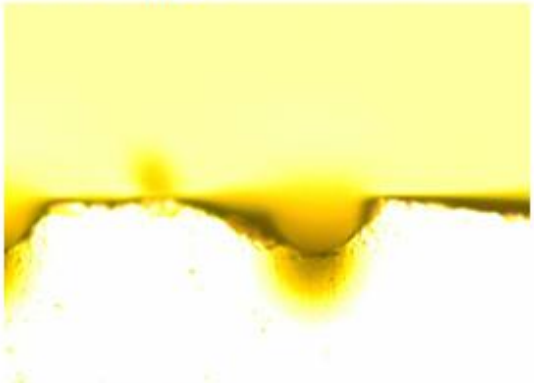

1.8mm/s

2.0mm/s

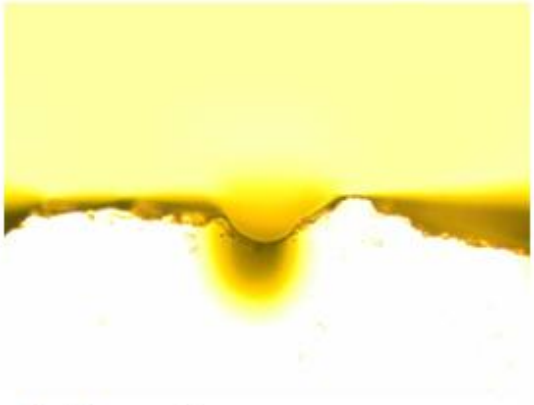

2.2mm/s

Pulse energy 65μJ

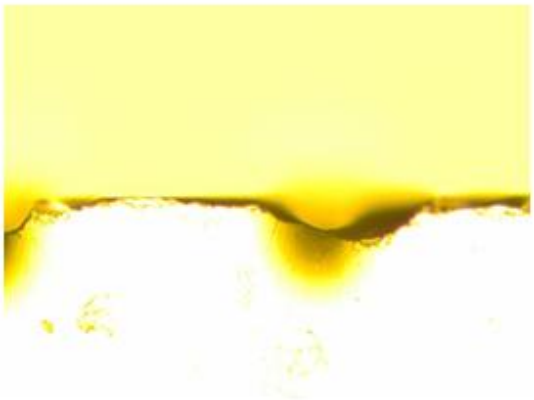

2.4 mm/s

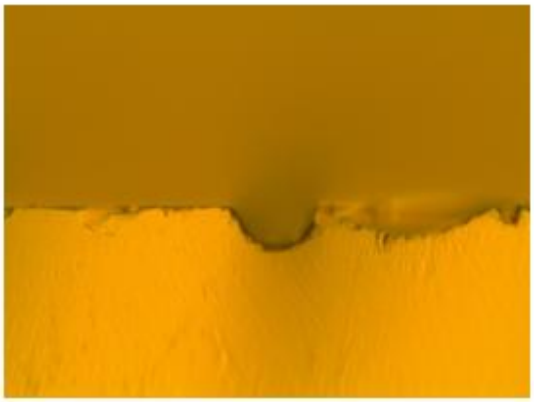

2.6 mm/s

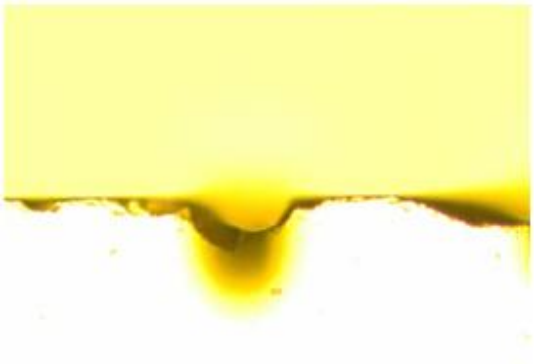

2.8 mm/s